國立臺灣大學電機資訊學院生醫電子與資訊學研究所

碩士論文

Graduate Institute of Biomedical Electronics and Bioinformatics

College of Electrical Engineering and Computer Science

National Taiwan University

Master's Thesis

結合自由流電泳與表面增強拉曼光譜
來進行多重分子檢測

Integration of Free Flow Electrophoresis and Surface-Enhanced Raman Scattering for multiplex biomolecule analysis

林明儁

Ming-Chun Lin

指導教授：黃念祖 博士

Advisor: Nien-Tsu Huang, Ph.D.

中華民國 113 年 7 月

July, 2024

doi:10.6342/NTU202401456

國立臺灣大學碩士學位論文
口試委員會審定書
MASTER'S THESIS ACCEPTANCE CERTIFICATE
NATIONAL TAIWAN UNIVERSITY

結合自由流電泳與表面增強拉曼光譜來進行多重分子檢測

（論文中文題目）(Chinese title of Master's thesis)

Integration of free flow electrophoresis and surface enhanced Raman scattering for multiplex biomolecule analysis.

（論文英文題目）(English title of Master's thesis)

本論文係 林明儁 (姓名) R10945040 （學號）在國立臺灣大學 生醫電資 (系/[✓ 所]/學位學程)完成之碩士學位論文，於民國 113 年 01 月 25 日承下列考試委員審查通過及口試及格，特此證明。

The undersigned, appointed by the Department / Institute of Biomedical Electronics and Bioinformatics on 25 (date) 01 (month) 2024 (year) have examined a Master's thesis entitled above presented by Ming-Chun, Lin (name) R10945040 (student ID) candidate and hereby certify that it is worthy of acceptance.

口試委員 Oral examination committee:

黃念祖 王玉麟 王俊凱

（指導教授 Advisor）

陳奕帆

系主任/所長 Director: 林致廷

doi:10.6342/NTU202401456

誌謝

在這段學術旅程的尾聲，我想借此機會向那些在我研究生涯中扮演重要角色的人表達誠摯的感謝。

首先，我要衷心感謝我的指導教授黃念祖教授。感謝您在研究方向上的指導與討論，雖然過程中常有激烈的辯論與磨練，但這些經歷促使我在實驗技巧與製圖能力上不斷精進。您對文辭的嚴格要求，提升了我的寫作精確性，雖然過程充滿挑戰與壓力，但也因此讓我的學術素養大幅提高。您的指導不僅體現在專業知識上，更體現了一種追求卓越的嚴謹態度。

我要感謝合作實驗室的師生們，特別是原分所的王玉麟老師、王俊凱老師、陳奕帆老師，以及赫文學長和欣玫學姊，感謝你們的專業知識、耐心指導以及在儀器與技術上的幫助，這些都為我的研究奠定了堅實的基礎。

此外，我要感謝實驗室的同學們，王鈞、子瑜、彥安，感謝你們在我實驗失敗時的建議和情感支持，啟耀、彥程、冠均、宣融，感謝你們在分擔實驗室的事務並配合我的需求。還有淮原，儘管進實驗室不久，已成為大家最可靠的後盾。你們的支持與鼓勵，特別是在每次會議討論中提出的有意見的建議，使我的研究更加完善。你們的陪伴和友誼，是我在這段艱辛旅程中的重要支柱。

最後，我要感謝我的家人。感謝你們無私的情感支持與經濟援助，讓我能夠全心投入學術研究。你們的支持是我克服困難、堅持不懈的力量源泉。

這段研究生涯充滿了挑戰與磨練，但正是這些經歷，讓我變得更加堅韌與成熟。感謝每一位在這段旅途中給予我幫助和支持的人。

doi:10.6342/NTU202401456

中文摘要

電泳是一種在各個領域被廣泛應用的樣品前處理技術。自由流電泳（FFE）是其中一種常見的電泳模式，因能連續且快速的進行分離，被用於細菌、蛋白質或DNA 的樣品純化和濃縮。近年來，由於降低人為錯誤和提高檢測準確性的潛力，自由流電泳與不同的偵測技術如電化學或是質譜儀的整合變得愈發受歡迎。然而，現有的整合方法面臨諸多限制，包括數據提供資訊不足、檢測時間較長和高成本等。為了應對這些挑戰，表面增強拉曼散射（SERS）因其高靈敏度和高特異性而備受矚目。在本篇論文中，我們開發了一個無縫整合 FFE 和 SERS 的多重分子檢測平台，可以在二十分鐘內完成樣本前處理與訊號檢測。我們首先通過使用不同電特性的三種螢光分子來評估平台的性能，驗證了此平台能夠成功分離並同時偵測與SERS 擁有不同親和力的分子。同時我們也透過模擬與實驗的交互驗證，建立了最佳的操作參數來進行分離。並且依據這樣的模擬公式，也能分析樣本的電特性，藉此獲得更多資訊。最後我們通過分離與檢測嘌呤的混合樣本證明了此平台能用於細菌分析，同時還能透過調整環境 pH 值來進行更廣泛的應用。FFE 與 SERS 的整合為同時檢測多種分子提供了一個具備了高靈敏度以及更快的處理速度的方法，有潛力應用於臨床診斷、環境監測和食品安全。

關鍵字：微流體系統、表面增強拉曼散射、自由流電泳、細菌檢測

doi:10.6342/NTU202401456

ABSTRACT

Electrophoresis is a widely used sample pre-processing technique in various fields. Free Flow Electrophoresis (FFE) is a common electrophoresis mode known for its continuous and rapid separation capabilities. It is applied in the purification and concentration of samples such as bacteria, proteins, or DNA. In recent years, integrating FFE with different detection techniques, such as electrochemistry or mass spectrometry, has gained popularity due to its potential to reduce human errors and enhance detection accuracy. However, existing integration methods face various limitations, including insufficient data information, prolonged detection times, and high costs. To address these challenges, Surface-Enhanced Raman Scattering (SERS) has garnered attention for its high sensitivity and specificity. In this thesis, we developed a seamlessly integrated platform that combines FFE and SERS for the detection of multiple molecules. This platform allows for sample pre-processing and signal detection to be completed within twenty minutes. We first evaluated the performance of the platform by using three fluorescent molecules with different electrical properties, confirming its ability to successfully separate and simultaneously detect molecules with varying affinities for SERS. Additionally, through the validation of simulations and experiments, we established optimal operational parameters for the separation process. By utilizing simulation formulas, we could analyze the electrical characteristics of the samples, providing more comprehensive information. Finally, we demonstrated the versatility of the platform by separating and detecting a mixed sample of purine derivatives, showcasing its potential for bacterial analysis. The platform's adaptability for broader applications was further highlighted by adjusting the pH value.

Keywords: Microfluidic system, SERS, Free flow electrophoresis, bacteria detection.

doi:10.6342/NTU202401456

CONTENTS

口試委員會審定書 .... #

誌謝 i

中文摘要 ii

ABSTRACT iii

LIST OF TABLES xii

Chapter 1 Introduction 1

1.1Electrophoresis for biomolecular separation 1

1.1.1 Electrophoresis type 1

1.1.2 μFFE for biomolecular separation 4

1.1.3 μFFE combined with detection method 9

1.2 SERS for biomolecular detection 11

1.2.1 SERS detection in microfluidics 11

1.2.2 Microfluidic SERS combined with separation method 14

1.3 Research Motivation 16

Chapter 2 Theory 18

2.1 Free flow electrophoresis theory 18

2.2 SERS theory 22

2.2.1 Principle of Raman scattering 22

2.2.2 Surface Enhancement Principle of SERS 23

2.3 Principal Component Analysis theory 25

Chapter 3 Materials and methods 28

3.1 System setup 28

3.1.1 System overview 28

doi:10.6342/NTU202401456

3.1.2 System design..........29

3.2 Fabrication protocols..........30

3.2.1 Microfluidic chip fabrication..........30

3.2.2 SERS substrate fabrication..........32

3.3 μFFE setup and process..........34

3.4 Optical setup..........35

3.5 Sample preparation..........36

3.6 Data analysis..........37

3.7 Revised experimental protocol..........38

3.7.1 Revised microfluidic chip fabrication..........40

3.7.2 Revised μFFE setup..........42

Chapter 4 Results and discussion..........43

4.1 Simulation results..........43

4.1.1 Sheath flow ratio verification..........43

4.1.2 Flow rate optimization..........45

4.2 Sample characterization and optimization..........46

4.2.1 Single sample FFE result..........46

4.2.2 SERS calibration curves..........47

4.3 Preliminary results..........49

4.4 Biomolecule FFE-SERS demonstration..........50

4.4.1 Mixing purine derivative quantification..........50

4.5 Results of the revised experimental protocol..........53

Chapter 5 Conclusions..........58

Chapter 6 Future works..........59

6.1 Integration of the system on the single chip..........59

6.1.1 Integration test results 60

6.2 Cell lysis component analysis..61

6.3 Analysis of bacteria due to external stimulation..62

References 64

doi:10.6342/NTU202401456

LIST OF FIGURES

Figure 1-1 The schematic of different types of electrophoresis. (A) Gel electrophoresis [1]. (B) Paper electrophoresis [2]. (C) Capillary electrophoresis [3]. (D) Free flow electrophoresis [4]. 1

Figure 1-2 The schematic of traditional free flow electrophoresis. (A) Resolution study of Microbial mixture separation [10]. (B) Evaluation of Separation Efficiency in Four FFE Methods [11]. (C) Purification of exosomes from cell culture media [12]..4

Figure 1-3 Modes of FFE [16]: (a) FFZE, (b) FFIEF, (c) FFITP, and (d) FFFSE.............5

Figure 1-4 Methods of preventing bubble: (A) Connection slits [19]. (B) Water-permeable gel or membrane chambers [20]. (C) Lower partition bars [21]....................6

Figure 1-5 Micro Free Flow electrophoresis for various analytes. (A) Fluorescent dye [26]. (B) Protein [31]. (C) DNA [30]. (D) Bacteria [36]. (E) Exosome [37]. (F) Medicine [40]. (G) Virus [41]..7

Figure 1-6 Micro Free Flow electrophoresis for sample separation/purification with different detection method. (A) The COMSOL simulation of the buffer inlet pressure [32]. (B) The schematic of μFFE device combined with the mass spectrometry [42]. (C) The schematic of μFFE with integrated partitioning bars [28]. (D) Quantification of propranolol in μFFE device [40]. (E) The electrophoresis focusing of myoglobin in μFFE device [34]. (F) The μFFE-gel chip to purify the virus [41]. (G) Layout of the electrophoretic enrichment chip. [35]..10

Figure 1-7 Microfluidic SERS detection modes. (A) Particle based [47]. (B) Substrate based [48]..13

Figure 1-8 Microfluidic SERS for various applications. (A) DNA [68]. (B) cancer [69].

doi:10.6342/NTU202401456

(C) Heavy metal [78]. (D) Pesticides [97]. (E) Melamine [121]. (F) Illegal food additive [105]. 13

Figure 1-9 Microfluidic SERS integrated with various separation methods. (A) Magnetic to detect cancer cells [124]. (B) Magnetic to detect pathogen [125]. (C) Membrane filtration to purify pathogen [126]. (D) Membrane filtration to detect pathogen [127]. (E) HPLC to detect pesticide [129]. (F) HPLC to detect purine derivatives [130]. (G) Capillary electrophoresis to detect riboflavin [131]. 16

Figure 2-1 Schematic of the FFE theory which presented with key parameters. d: The deflection distance along y axis from inlet to outlet; W_{ch}: The width of the FFE channel; L_{ch}: The length of the FFE channel; Plus/minus signal: Applied electric field; $v_{sa,e}$: The velocity of the sample resulting from the electric field; $v_{sa,f}$: The velocity of the sample resulting from the flow field. F_x: The force acting on the sample along the x-axis; F_y: The force acting on the sample along the y-axis. The gray band represents the trajectory of the negatively charged sample. 18

Figure 2-2 Schematic energy diagrams of various scattering [133]. 23

Figure 2-3 The Representative mechanisms of SERS [136]. (A) Electromagnetic enhancement. (B) Chemical enhancement. 25

Figure 2-4 The illustration of the charge transfer mechanism [135]. 25

Figure 2-5 The schematic of the PCA process [138]. 27

Figure 2-6 The example figure of the (A) PCA. (B) PVE. 27

Figure 3-1 The schematic of the FFE-SERS system. 28

Figure 3-2 The design of the PDMS channel. (A) For μFFE (B) For SERS; The actual pictures of the PDMS chip. (C) μFFE (D) SERS. 29

Figure 3-3 The actual picture related to the PMMA mold. (A) The processed PMMA mold. (B) CNC machine, which model is Roland MDX-50....................................31

Figure 3-4 Schematic of the μFFE-SERS device fabrication procedure.........................32

Figure 3-5 The schematic of the silver-filled AAO substrates [142]..............................33

Figure 3-6 The SEM image of silver-filled AAO substrate. (A) before growth (B) after growth of silver nanoparticles [142]..33

Figure 3-7 The experiment setup on the Raman microscope. 35

Figure 3-8 The actual picture of the (A) Inverted microscope. (B) Raman microscope. 36

Figure 3-9 The example figures of the fluorescence image measurement under (A) bright field and (B) fluorescent field. The green line represents the measurement location. 38

Figure 3-10 (A) The schematic of the revised FFE-SERS system. The actual pictures of the PDMS chip. (B) μFFE (C) SERS. 39

Figure 3-11 The revised design of the PDMS channel for μFFE...................................39

Figure 3-12 The image of the fabricated mold. 41

Figure 4-1 The COMSOL result of the sample concentration under different ratios of buffer and sample flow. (A) Sheath flow verification. (B) Flow rate optimization. Q_b: flow rate of buffer. Q_s: flow rate of the sample................45

Figure 4-2 The COMSOL result of the surface plot for (A) streamline (B) velocity (C) pressure under $Q_b : Q_s = 60 : 2$ μL/min situation. 46

Figure 4-3 The μFFE result and intensity diagram of (A) Fluorescein (B) Rhodamine B (C) R6G. The green line represents the measured coordinate. 47

Figure 4-4 The SERS spectrum of fluorescent dye. (A) Fluorescein. (B) Rhodamine B. (C) Rhodamine 6G. The standard curve of (D) Fluorescein. (E) Rhodamine B. (F) Rhodamine 6G. The dashed line represents the peak value for

doi:10.6342/NTU202401456

calibration. 48
Figure 4-5 The proof-of-concept result for three fluorescent dyes flowed into the FFE-SERS system. The fluorescent image under (A) 0 V. (B) 150 V. The SERS spectrum under (C) 0 V (D) 150 V. (E) PCA result of the SERS spectrum from five outlets of the FFE channel under 150 V. 50
Figure 4-6 The SERS spectrum of purine derivatives. (A) Adenine. (B) Uracil. The standard curve of (C) Adenine. (D) Uracil. The dashed line represents the peak value for calibration. 52
Figure 4-7 The FFE results for purine mixing under (A) 0 V and (B) 150 V; The comparison of peak intensities at Raman shifts of (C) 733 cm^{-1} (D) 800 cm^{-1} between 0 V and 150 V. 52
Figure 4-8 The COMSOL result of the sample concentration for (A) Microfluidic stability verification. (B) Sheath flow verification (C) Flow rate optimization. Q_b: flow rate of buffer. Q_s: flow rate of the sample. The red square represents the chosen parameter. 54
Figure 4-9 The μFFE result and intensity diagram of (A) Fluorescein (B) Rhodamine B (C) R6G. The green line represents the measured coordinate. 55
Figure 4-10 The proof-of-concept result for three fluorescent dyes flowed into the FFE-SERS system. The fluorescent image under (A) 0 V. (B) 24 V. The SERS spectrum under (C) 0 V (D) 24 V. (E) PCA result of the SERS spectrum from five outlets of the FFE channel under 24 V. 56
Figure 4-11 The SERS spectrum of purine derivatives. (A) Uric acid. The standard curve of (B) Uric acid. The dashed line represents the peak value for calibration.56
Figure 4-12 The FFE results for purine mixing under (A) 0 V and (B) 24 V; The comparison of peak intensities at Raman shifts of (C) 733 cm^{-1} (D) 1130 cm^{-}

doi:10.6342/NTU202401456

^{1} between 0 V and 24 V. 57

Figure 6-1 The schematic of the integration single chip. The gray square represents the glass slide, while the purple region indicates the deposition of silver nanoparticles. 59

Figure 6-2 Image of the PDMS channel directly bonded to the SERS substrate (A) Initial state (B) After applying 25 V for 15 minutes. 60

Figure 6-3 Image of the SERS substrate which is an etching by the NaOH (A) Initial state (B) After applying 25 V for 15 minutes. 61

Figure 6-4 SERS spectra for cancer cells with and without lysis. Specific peaks denote presumed organic matter [152]. 62

Figure 6-5 Schematic diagram of a black-box approach for bacterial differentiation [153]. 63

doi:10.6342/NTU202401456

LIST OF TABLES

Table 1-1 Summarize of the current μFFE techniques. 8

Table 3-1 The microfluidic channel parameters. 30

Table 3-2 The microfluidic channel parameters for the new design. 40

Table 4-1 The parameters for COMSOL simulation. 43

doi:10.6342/NTU202401456

Chapter 1 Introduction

1.1 Electrophoresis for biomolecular separation

1.1.1 Electrophoresis type

Electrophoresis is a foundational laboratory technique utilized for the separation of molecules based on their electrical charge and size. This versatile method holds a pivotal position in various scientific domains, encompassing biology, biochemistry, and chemistry. Electrophoresis can be categorized based on the presence or absence of a supporting medium. The former category comprises gel electrophoresis and paper electrophoresis, while the latter category encompasses free-flow electrophoresis and capillary electrophoresis, the schematic is shown in Figure 1-1.

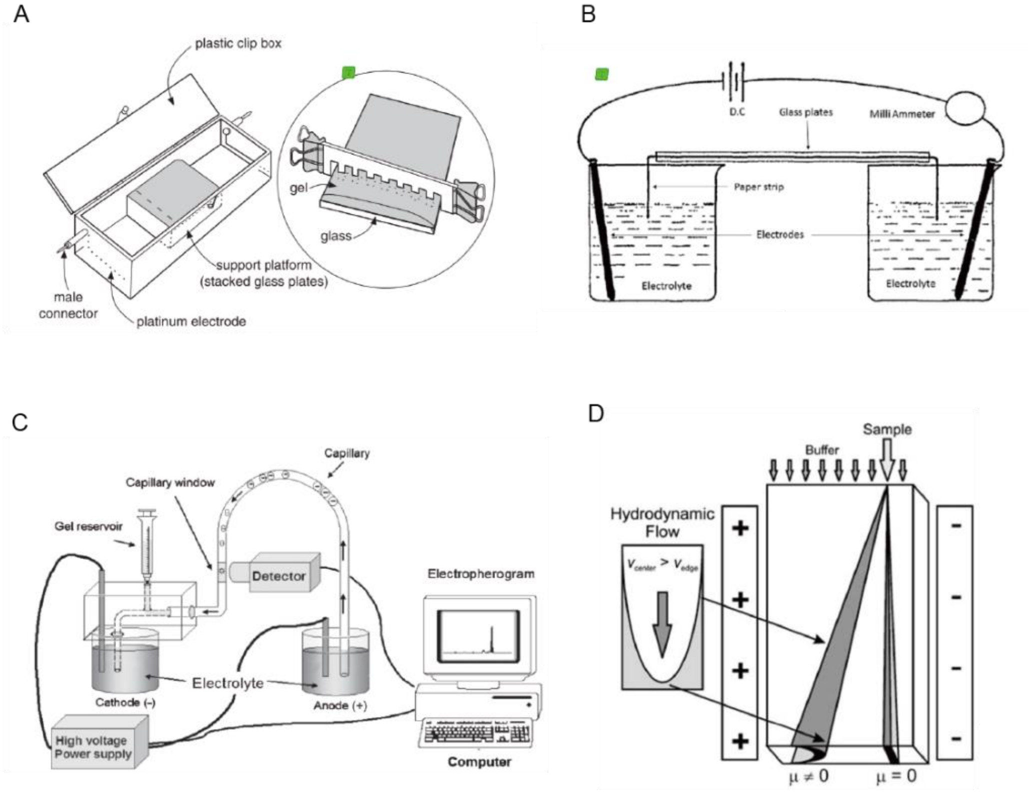

Figure 1-1 The schematic of different types of electrophoresis. (A) Gel electrophoresis [1]. (B) Paper electrophoresis [2]. (C) Capillary electrophoresis [3]. (D) Free flow electrophoresis [4].

Gel electrophoresis is a highly prominent technique in the field of electrophoresis. It utilizes a gel matrix, typically crafted from materials such as agarose, commonly employed for DNA and RNA analysis, or polyacrylamide, which is used for protein separation [5]. The prepared gel solution is loaded into the gel slab and allowed to cool. Next, the analytes are injected from one side of the gel, which is covered with the running buffer. Voltage is then applied to facilitate the migration of the analytes [1]. In contemporary applications, two-dimensional gel electrophoresis is extensively utilized in proteomics. This advanced method allows for the detection and separation of complex mixtures of molecules based on their isoelectric point and molecular weight. For instance, David Rouquié *et al*. utilized this technique to investigate whether soybean food allergens exhibit higher levels in genetically modified species [6].

To perform paper electrophoresis, first prepare the filter paper strips and the electrophoresis buffer solution with the required pH and ionic strength. Then, wet the filter paper with the buffer to create a conductive path. Carefully apply the samples to the spotting zone or sample application wells. When voltage is applied to the electrodes in the buffer solution, the charged molecules will migrate through the paper strip based on their charge and size [2]. Paper electrophoresis saw a decline after 1950 due to its lower sensitivity and resolution compared to other separation methods like gel or capillary electrophoresis. However, this technology made a resurgence in research with the development of Microfluidic Paper-based Analytical Devices (µPADs), offering advantages such as affordability and the absence of a need for pumps [2]. For example, C. L. S. Chagas *et al.* developed a paper-based microchip electrophoresis device equipped with integrated hand-drawn pencil electrodes for conductivity detection. They successfully showcased the device's capability to separate albumin and creatinine, which serves as evidence of kidney failure within a mere 150 seconds [7].

doi:10.6342/NTU202401456

Capillary electrophoresis (CE) is a high-resolution technique that utilizes a narrow capillary tube filled with an electrolyte solution. When an electric field is applied, charged molecules migrate through the capillary, with smaller molecules moving more swiftly [3]. In most cases, when referring to capillary electrophoresis (CE), we are specifically discussing capillary zone electrophoresis (CZE), a technique that operates without a support medium. K. Zamuruyev *et al*. have described an automated capillary electrophoresis platform combined with ESI-MS. They successfully separated a mixture of amino acids using their automated CE system [8]. Within the realm of CE, various specialized methods are available, including capillary gel electrophoresis (CGE), which employs a liquid gel within the capillary tube. CGE is particularly useful for separating biopolymers with a consistent charge-to-size ratio. This method offers superior resolution and faster separation compared to traditional gel-based techniques. For instance, M. Wand *et al.* utilized CGE to separate different topological plasmids, with supercoiled plasmids being the most efficient for eukaryotic transfection, making them valuable for gene therapy applications [9].

Free-flow electrophoresis (FFE) is a separation technique where charged particles in a liquid medium move in a vertical electric field [4]. This continuous flow system enables separation based on charge-to-size ratios, offering advantages like continuous separation, integrated detection systems, sample harmlessness, and multifaceted data generation. For example, Scott Ramsey *et al.* extensively examined the impact of FFE properties, such as pH value, viscosity, or salt concentration, on the separation efficiency of microbial mixtures [10]. They concluded that different bacteria exhibit distinct electrophoretic mobility depending on the experimental conditions and compared their findings with the Helmholtz-Smoluchowski equation, which calculates substance mobility in the liquid phase. In another study, Reinhard Kuhn et al. employed four types of FFE to purify enzymes from E. coli cell extracts, summarizing purity and throughput relative to each type [11]. Notably, in 2020, Simon Staubach et al. utilized FFE to purify exosomes from cell culture media [12]. They

doi:10.6342/NTU202401456

utilized conditioned media from human bone marrow-derived MSCs, implementing a pH gradient for Free-Flow Electrophoresis (FFE) separation. Subsequently, they quantified CD9+ entities, identified by the exosome biomarker, across a total of 96 fractions. Figure 1-2 illustrates the schematic representation of these discoveries.

Nevertheless, traditional FFE comes with limitations, including a labor-intensive workflow, bulky devices, and challenges in separation efficiency, such as joule heating, long residence time, and the need for substantial amounts of reagents [13]. To overcome these drawbacks, the microfluidic free-flow electrophoresis (µFFE) has been introduced.

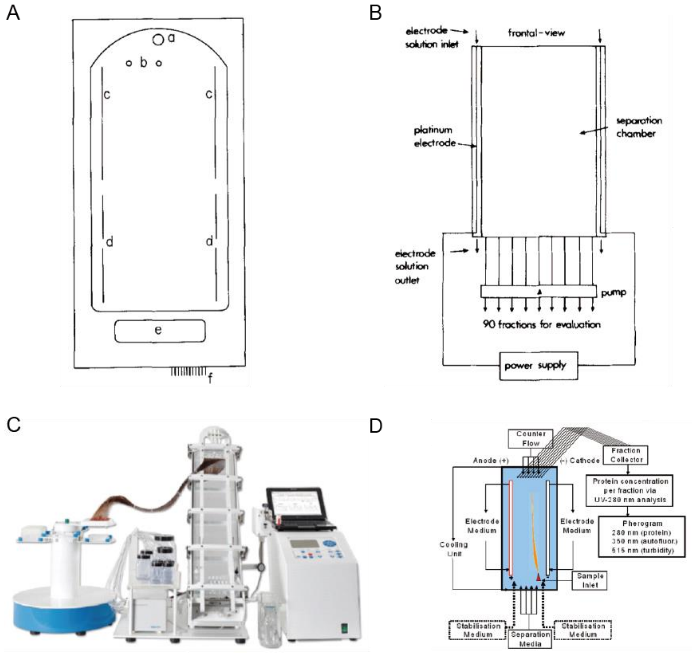

Figure 1-2 The schematic of traditional free flow electrophoresis. (A) Resolution study of Microbial mixture separation [10]. (B) Evaluation of Separation Efficiency in Four FFE Methods [11]. (C) Purification of exosomes from cell culture media [12]

1.1.2 µFFE for biomolecular separation

Micro Free Flow Electrophoresis (µFFE) was first applied by Raymond *et al* in 1994 [14]. With the help of miniaturization, faster heat dissipation, less residence time, reagents and sample requirements can be realized [13]. In summary, µFFE typically has dimensions

doi:10.6342/NTU202401456

in the range of a few centimeters in width and length, with a height at the micrometer level [15]. In these dimensions, the residence time for electrophoresis is typically less than five minutes. The system can be constructed from various materials, including glass, PDMS, and PMMA [16]. Glass offers high reliability over a broad pH range and under high pressure, along with optical transparency for easy observation. However, the complex and costly fabrication process and the fragile structure are drawbacks. PDMS provides advantages such as good gas permeability, relatively low cost, easy fabrication, and elasticity. Yet, the elasticity may lead to sagging in the separation chamber under external pressure. PMMA is known for its great machinability and high mechanical resistance, but it comes with the disadvantage of lower precision in μFFE device fabrication [17].

There are four common modes of μFFE: (1) free-flow zone electrophoresis (FFZE), (2) free-flow isoelectric focusing (FFIEF), (3) free-flow isotachophoresis (FFITP), and (4) free-flow field step electrophoresis (FFFSE) [16]. Figure 1-3 illustrates the schematic of these different modes. In summary, these four modes differ in the buffer injection method and option. FFZE injects one kind of buffer into the flow zone, maintaining a constant pH value and separating analytes solely based on their electrophoretic mobility. In contrast, FFIEF generates a pH gradient in the flow zone, concentrating analytes based on their isoelectric point. FFITP injects leading and terminating buffers with higher and lower electrophoretic mobility compared to the analytes, centralizing them in these two buffers. FFFSE introduces a less conductive buffer in the center of the flow zone, drastically reducing the analyte electrophoretic velocity and concentrating the components.

doi:10.6342/NTU202401456

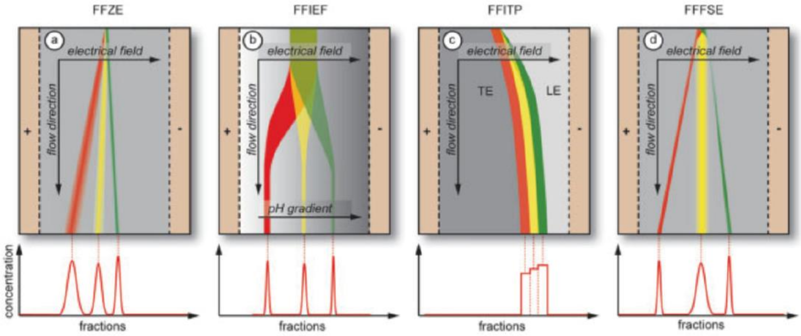

Figure 1-3 Modes of FFE [16]: (a) FFZE, (b) FFIEF, (c) FFITP, and (d) FFFSE.

In microfluidic systems like μFFE, preventing electrolysis-generated bubbles from penetrating the main channel is crucial for maintaining separation efficiency (Figure 1-4) [18]. Electrolysis bubbles, larger and more challenging to remove in miniaturized systems than in traditional electrophoresis, can impact separation outcomes. Strategies to address this issue include incorporating connection slits [19], water-permeable gel chambers or membranes [20], or lower partition bars than the main channel [21]. These designs act as barriers, hindering bubble penetration while facilitating the electrolyte exchange necessary for sustaining the electric field in electrophoresis. Such innovations help enhance the reliability and effectiveness of microfluidic separation techniques.

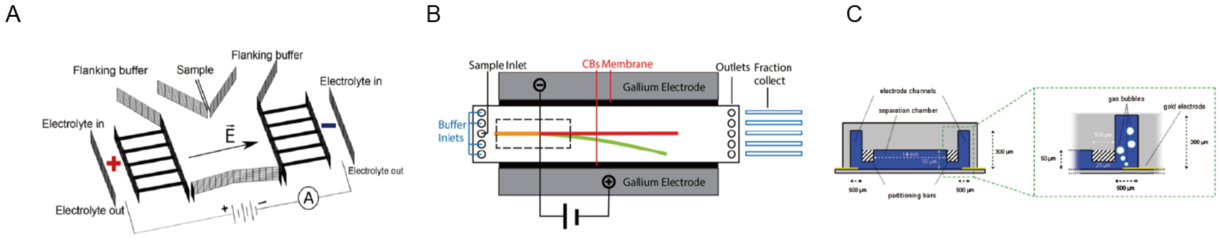

Figure 1-4 Methods of preventing bubble: (A) Connection slits [19]. (B) Water-permeable gel or membrane chambers [20]. (C) Lower partition bars [21].

μFFE is applicable to various analytes, including fluorescent dye [14,19-29], proteins [27,30-34], DNA [30], bacteria [10,11,35,36], exosomes [12,37], medicines [38-40], and viruses [41]. T. W. Herling *et al.* quantified the net solvated charge of fluorescent molecules using a single photolithography step chip, assessing different buffer types and concentrations (Figure 1-5 A) [26]. E. Poehler *et al.* employed FFIEF with NIR fluorescence to determine the isoelectric point of biomolecules, comparing results to mass spectrometry (Figure 1-5B) [31]. P. Novo *et al.* efficiently lowered µFFE fabrication difficulty using an ionic permeable membrane and FFIZE for DNA separation (50-1500 base pairs) (Figure 1-5C) [30]. J. E. Prest *et al.* used FFITP to separate *E. herbicola* from a new coccine medium, successfully concentrating bacteria into one outlet among nine (Figure 1-5D) [36]. F. Barbaresco *et al.* introduced a 3D printed chip for 50 nm exosome separation, achieving differentiation from 500 nm nanoparticles at 40V (Figure 1-5E) [37]. T. Haensch *et al.* integrated an impedimetric sensor for in-situ detection in a lab-on-chip system, recording impedance changes during analyte passage (Figure 1-5F) [40]. Additionally, researchers like M. Hügle *et al.* utilized µFFE to deflect and agarose gel to isolate viruses from the medium, achieving substantial purification (Figure 1-5G) [41]. Table 1-1 summarizes the current study of the µFFE which analyzes different samples with the important parameters.

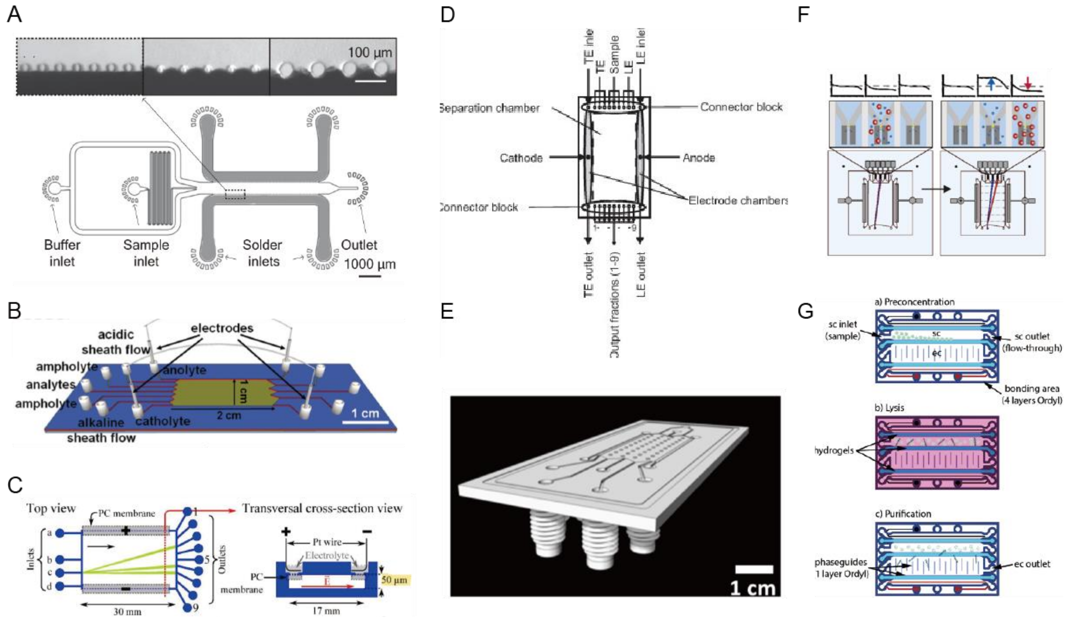

Figure 1-5 Micro Free Flow electrophoresis for various analytes. (A) Fluorescent dye [26]. (B) Protein [31]. (C) DNA [30]. (D) Bacteria [36]. (E) Exosome [37]. (F) Medicine [40]. (G) Virus [41]

Table 1-1 Summarize of the current μFFE techniques.

Analytes	Chip Material	Bubble Prevention	Chip Dimensions (h*w*l) (mm)	Flow rates (μL/min)	Applied Voltage	Residence time	Detection Method	Application	Refs
Fluorescein Rhodamine B, 6G, 116	Glass PDMS Polycarbonate	Partition bars	0.05*2.8*11	42 (sample)	110 V	2.2 min	Fluorescence	None	[28]
DNA ladder protein pI marker	PDMS Glass	Polycarbonate membranes	0.05*17*30	40 (buffer) 2 (sample)	50V	0.85 min	Fluorescence BCA assay	DNA separation	[30]
Myoglobin	Glass	Connection channels	0.02*4.4*12.2	5 (buffer) 5 (sample)	210V	None	SERS	Protein concentration	[34]
Bacteria	Pyrex wafer	Bubble expulsion Structure	0.12*11*22	3 (sample)	50V	5.6 min	Spread plate method	Bacteria purification	[35]
Exosome	PMMA	Partition bars	0.1*13*30	20 (buffer) 10 (sample)	55V	1.3 min	UV-Vis DLS	Exosome purification	[37]
Propranolol	Fused silica	Hydrogel barrier	0.2*15*20	20 (buffer) 0.5 (sample)	400V	2.9 min	Electro-chemical Impedance	Medicine detection	[40]
bacteriophage	Glass	gel barrier Flushed buffer	1.12*16*27	5 (sample)	120V	40 s	qPCR	Virus concentration	[41]
Fluorescent dye Melamine	PDMS Glass	gel barrier Flushed buffer	0.15*10*30	60 (buffer) 2 (sample)	150V	0.75 min	Fluorescence SERS	Heavy metal detection	This work

1.1.3 μFFE combined with detection method

After the separation process, detecting the separated molecules is a crucial aspect of μFFE techniques [18]. Figure 1-6 concludes the common detection methods employed in μFFE techniques. Some studies employ offline detection methods like qPCR (Figure 1-6F) [41] or the plating method (Figure 1-6G) [35]. These methods involve extracting the separated sample from the chip for further experimentation. While this approach simplifies device setup, it requires more experimental procedures. In current μFFE research, the emphasis is on on-chip detection, enabling a single streamlined process for both separation and detection. Integrated detection methods include mass spectrometry, fluorescent imaging, Electrochemical Impedance Spectroscopy, and SERS detection.

Mass spectrometry offers the advantage of detailed, label-free information, but it requires a long detection time and involves bulky, expensive devices. For example, M. Jender *et al.* used a PMMA microfluidic chip to separate AMP, ATP, and CoA, enabling real-time detection using mass spectrometry (Figure 1-6B) [42]. Fluorescence is the most commonly employed method for μFFE, offering good spatial resolution. Nevertheless, it involves a complex optical setup and requires labeling. S. Köhler *et al.* utilized a custom-made three-layer PDMS chip to separate fluorescent dye and labeled amino acids, marking the first instance of incorporating partitioning bars in a μFFE system (Figure 1-6C) [28]. Electrochemical detection boasts advantages such as a fast, simple setup and a relatively inexpensive chip. However, it provides data in only one dimension, limiting its ability to offer comprehensive sample information. T. Haensch *et al.* incorporated an impedimetric sensor for in-situ detection in the lab-on-chip system. The recorded impedance decreases as the charged propranolol traverses the detection region, whereas the neutral buffer or precursor analytes cause an increase in impedance (Figure 1-6D) [40].

doi:10.6342/NTU202401456

To overcome the challenges mentioned earlier, SERS detection was considered. SERS offers detailed information, relatively high sensitivity, and a short detection time [43]. M. Becker *et al.* have shown that they can apply the Isotachophoretic free-flow electrophoretic focusing to concentrate the myoglobin into specific channels and detect them by the SERS (Figure 1-6E) [34]. Nonetheless, their findings still have limitations, including the demanding optimization process, clogging issues resulting from particle-based SERS detection, and a lack of multiple analyte demonstrations.

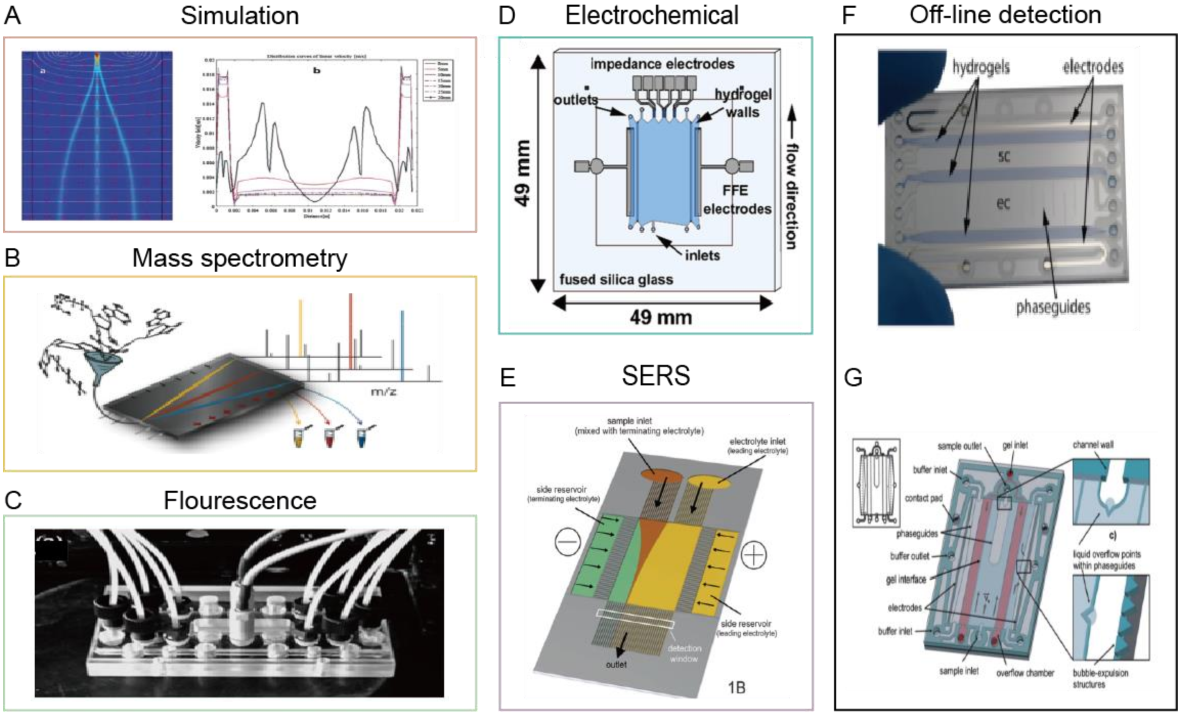

Figure 1-6 Micro Free Flow electrophoresis for sample separation/purification with different detection method. (A) The COMSOL simulation of the buffer inlet pressure [32]. (B) The schematic of µFFE device combined with the mass spectrometry [42]. (C) The schematic of µFFE with integrated partitioning bars [28]. (D) Quantification of propranolol in µFFE device [40]. (E) The electrophoresis focusing of myoglobin in µFFE device [34]. (F) The µFFE-gel chip to purify the virus [41]. (G) Layout of the electrophoretic enrichment chip. [35].

doi:10.6342/NTU202401456

1.2 SERS for biomolecular detection

1.2.1 SERS detection in microfluidics

Surface-Enhanced Raman Spectroscopy (SERS) is an optical detection method that leverages metallic nanostructures, such as gold or silver nanoparticles, to amplify the Raman scattering signal of molecules, resulting in enhancement factors of up to 10^{14} [44]. It has emerged as a powerful analytical tool for highly sensitive and specific molecule detection, providing label-free fingerprint detection. However, traditional SERS face limitations such as high dosage requirements, low efficiency, and imprecise process control. To overcome these challenges, microfluidics has been introduced to integrate with SERS, offering low volume and precise fluid control [45].

There are two types of microfluidic SERS detection methods: collide-based and substrate-based [46]. The first invention is collide-based, where gold or silver nanoparticles are added with the analytes to generate Raman signal enhancement. This method is favored by researchers lacking the ability to fabricate sophisticated substrates. For instance, H. Lu *et al*. studied a microfluidic channel to facilitate analyte entry into "hot spots" for enhanced SERS sensitivity (Figure 1-7A) [47]. They developed a cascaded splitting and recombination micro-mixer before the detection region, achieving a limit of detection (LOD) of 9E-11 M with R6G as the analyte. However, aggregation issues and poor signal consistency are significant drawbacks. Also, determining the concentration between nanoparticles and analytes before the experiment increases process time.

On the other hand, substrate-based methods are popular due to their ability to control the size and shape of nanostructures, providing high reproducibility and higher enhancement factors. For example, G. Chen *et al*. reported a method for fabricating an Ag nanodot array microfluidic SERS chip to achieve multiplex low-concentration analyte

doi:10.6342/NTU202401456

detection (Figure 1-7B) [48]. They evaporated Ag on the AAO and covered these substrates with a PDMS channel. Finally, they used adenine and thiram mixing solutions as analytes, claiming the ability to measure concentrations of 5E-7 M and 5E-6 M, respectively.

Microfluidic SERS finds applications in various fields such as biomedical sensing, environmental monitoring, and food safety. In biomedical sensing, it is utilized for bio-nanoparticle detection, including antigen [49-55] or DNA [56-62] sensing, and cancer [55,56,63-66] detection. For instance, H. T. Ngo *et al.* employed the Molecule Sentinel-on-Chip technique to detect the RSAD2 gene (Figure 1-8A) [67]. This technique immobilizes the molecule sentinel probe on the nano wave chip, enabling the detection of target DNA with SERS. The results indicate that complementary DNA exhibits a lower SERS signal compared to the blank and non-complementary ones, demonstrating the technique's capability to detect specific DNA sequences. Another example by Z. Wang *et al.* involved the use of magnetic beads coated with a gold layer, decorated with the aptamer of CD63, a crucial biomarker on the exosome surface (Figure 1-8B) [68]. They confirmed the ability to detect tens of exosomes, such as SKBR3 or T84, per microliter in a blood sample.

In environmental monitoring [69], SERS is frequently applied for heavy metal detection [46,70-78], pharmaceuticals [79-88], and pesticides [89-95]. For example, S. Yan *et al.* developed Ag nanostructures in a microfluidic channel via an electroless galvanic displacement reaction, reducing fabrication time and process complexity compared to another research (Figure 1-8C) [77]. This platform was used to detect Hg ions in water, achieving a limit of detection (LOD) of 1E-7M. Another example by G. E. Alt *et al.* demonstrated the application of pesticides. The designed microfluidic channel combined the synthesis of nanoparticles, adsorption of an analyte, and detection zone

doi:10.6342/NTU202401456

(Figure 1-8D) [96]. They calibrated the glyphosate concentration in tap water samples, reaching a LOD of 40 μg/L.

Regarding food safety [97], common analytes for SERS include chemicals in animal production [98-104], illegal food additives [100,105-111], and foodborne pathogens [112-119]. For example, M. Viehrig *et al.* developed a reusable SERS substrate with the assistance of electrochemistry (Figure 1-8E) [120]. They fabricated Au-capped nanopillars that could attract or repel analytes depending on the applied voltage, making the substrate reusable. They achieved a LOD of 2 ppm for melamine in diluted milk. Additionally, S. H. Yazdi *et al.* developed a compact system eliminating the need for a syringe pump, claiming they could reach a LOD of 5 ppm for methyl parathion, 0.1 ppb for malachite green, and 5 ppb for thiram simultaneously (Figure 1-8F) [104].

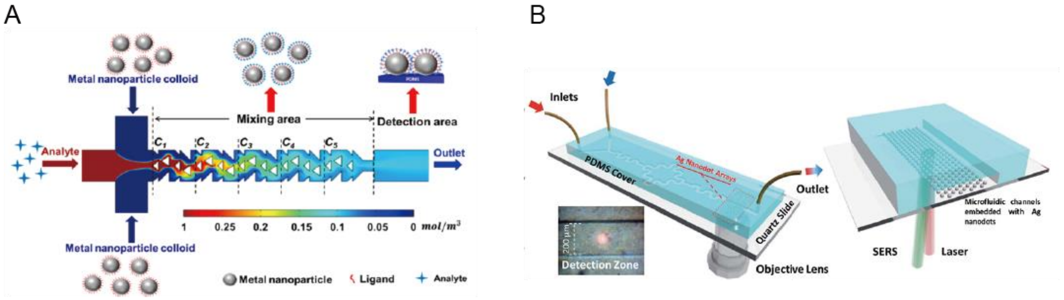

Figure 1-7 Microfluidic SERS detection modes. (A) Particle based [47]. (B) Substrate based [48].

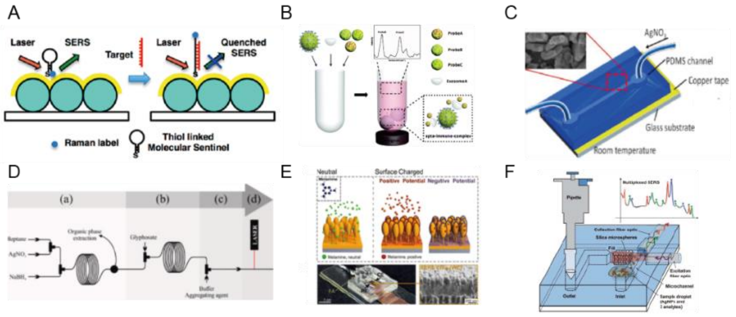

Figure 1-8 Microfluidic SERS for various applications. (A) DNA [67]. (B) cancer [68]. (C) Heavy metal [77]. (D) Pesticides [96]. (E) Melamine [120]. (F) Illegal food additive [104].

1.2.2 Microfluidic SERS combined with separation method

SERS encounters certain limitations when dealing with complex samples, such as a low signal-to-noise ratio and spectral interference from other molecules present in the sample [121]. To address these challenges, combining separation methods with SERS has been proposed to overcome the limitations of SERS in analyzing complex samples. Four major separation methods have been incorporated with SERS: magnetic, membrane filtration, chromatography, and electrophoresis [122].

Magnetic separation is widely used in combination with SERS. Commonly used magnetic materials, such as Fe3O4 and γ-Fe2O3, possess a large specific area to adhere to analytes [122]. Researchers use external magnetic force to attract analytes from the background solution, enabling clear detection by SERS. For instance, P. Reokrungruang *et al.* describe a cost-effective plasmonic paper as a SERS substrate, using carboxylated magnetic particles to separate colorectal cancer cells (HT-29) from a mixture of non-target fibroblasts, achieving over 80% cell capture (Figure 1-9A) [123]. Another example by Y. Wang *et al.* applies silica-coated magnetic probes functionalized with specific pathogen antibodies from a food matrix, with a LOD of *Staphylococcus aureus* in peanut butter reaching 10^3 CFU/mL (Figure 1-9B) [124]. However, this technique often requires labeled magnetic particles and can be challenging to incorporate into microfluidic systems.

Membrane filtration is another technique for separating analytes based on pore size or selective permeable membranes, which filter analytes using external forces such as gravity or pressure [122]. This method improves product quality and reduces risk factors. For example, K. R. Wigginton *et al.* employ a polycarbonate track-etched membrane filter to isolate *G. lamblia* from a water sample, achieving a capture rate of about 95% (Figure 1-9C) [125]. Another example by I. H. Cho et al. detects low levels of *E. coli* O157:H7

doi:10.6342/NTU202401456

using membrane filtration, reaching a detection limit of 10 CFU/mL in ground beef samples after 3 hours of separation (Figure 1-9D) [126]. However, this method's stability is compromised due to the fragile nature of the membrane, potentially causing analyte loss.

Chromatography relies on differential affinities between substances in a mobile phase and a stationary phase [127]. As the sample travels through the stationary phase, distinct components separate based on their interaction strengths, ensuring precise and sensitive separation for quantitative analysis. For instance, W. Wang *et al.* combined HPLC and SERS for the rapid detection of thiram, achieving a LOD of 10^{-7} mol/L in pure thiram samples (Figure 1-9E) [128]. Another study by Y.Y. Wang *et al.* applied an automatic fluid control system to manipulate the mixing of purine derivatives (Figure 1-9F) [129]. With HPLC separation and SERS substrate detection, they utilized the compact system directly on the Raman microscope, quantifying hypoxanthine and adenine simultaneously in the 10^{-6} M range. However, the drawbacks of chromatography include complexity and time-consuming procedures.

Electrophoresis has the advantage of label-free separation and harmlessness to analytes. Consider electrophoresis, both capillary electrophoresis and free flow electrophoresis (FFE) have been incorporated with SERS. Capillary electrophoresis utilizes a long tube, and analytes with different charge-to-size ratios migrate at different speeds under an applied electric field. For example, A. Tycova *et al.* developed a capillary electrophoresis microfluidic chip combined with SERS particle-based detection (Figure 1-9G) [130]. Mixing analytes are injected into the chip and migrate with applied voltage; downstream of the chip, gold nanoparticles mix with analytes and are detected by SERS. They demonstrated the purification of riboflavin in BBQ sauce. However, capillary electrophoresis requires very high electric fields (thousands of Volts) and relatively long

doi:10.6342/NTU202401456

processing times compared to FFE, and the separated analytes cannot be used for further experiments due to temporal separation. While we discussed the study incorporating FFE and SERS detection earlier (Figure 1-6E) [34], it still has some limitations such as limited application and several preprocessing steps.

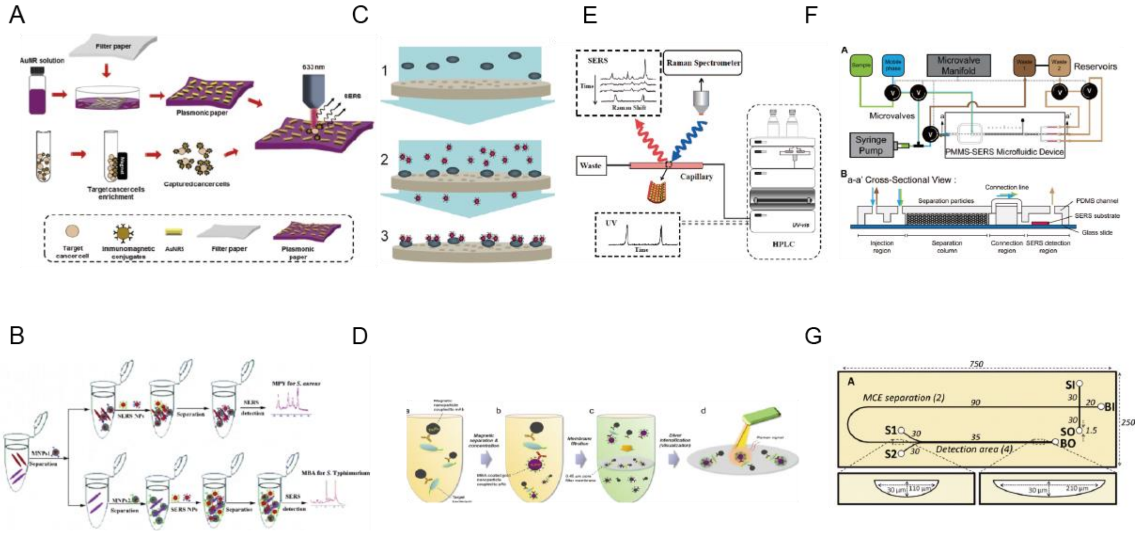

Figure 1-9 Microfluidic SERS integrated with various separation methods. (A) Magnetic to detect cancer cells [123]. (B) Magnetic to detect pathogen [124]. (C) Membrane filtration to purify pathogen [125]. (D) Membrane filtration to detect pathogen [126]. (E) HPLC to detect pesticide [128]. (F) HPLC to detect purine derivatives [129]. (G) Capillary electrophoresis to detect riboflavin [130].

1.3 Research Motivation

The integration of biomolecular separation and detection has become increasingly popular due to its potential to reduce human error, shorten experiment times, and enhance detection accuracy [131]. µFFE emerged as a promising technique for analyte preprocessing. It requires low volume, seamlessly integrates into microfluidic systems, and poses no harm to samples, facilitating the generation of multiple data points [13]. While several detection methods can integrate with µFFE, limitations persist, including insufficient data information with methods like fluorescence [28] or electrochemical impedance [40] and the extended detection time and cost associated with mass spectrometry [42].

To address these challenges, our research aims to design a platform that seamlessly integrates μFFE with a SERS substrate. This study introduces three unique features: (1) Integration of separation based on electrophoretic mobility and optical detection into a single streamlined process. (2) Catering to the demand for low analyte volumes, high processing speed, and detailed analyte information. (3) Implementation of an automatic fluid control system, mapping system for obtaining multiple analyte information, and quantification of analyte concentrations. With these features, we aim to minimize human error, save costs and time when analyzing biological samples such as bacteria or proteins. Furthermore, the detailed analyte information could enable us to analyze complicated samples such as bacteria supernatants, as different analytes may be separated based on their electrical properties.

Chapter 2 Theory

2.1 Free flow electrophoresis theory

FFE's theory is founded on the principle of achieving equilibrium between the drag force and the electric force [4], which arise from the flow and electric field, respectively. In this section, our objective is to validate this theory. By substantiating the theory, we can theoretically optimize the parameters involved. Figure 2-1 shows the schematic of the FFE channel with the external electric field and laminar flow field.

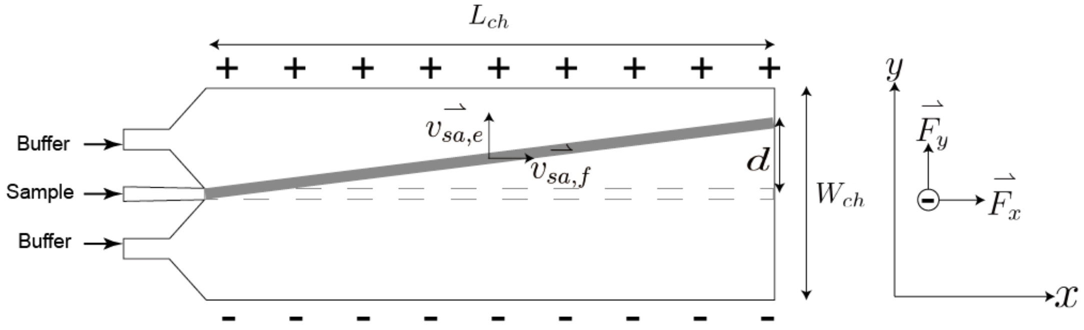

Figure 2-1 Schematic of the FFE theory which presented with key parameters. d: The deflection distance along y axis from inlet to outlet; W_{ch}: The width of the FFE channel; L_{ch}: The length of the FFE channel; Plus/minus signal: Applied electric field; $v_{sa,e}$: The velocity of the sample resulting from the electric field; $v_{sa,f}$: The velocity of the sample resulting from the flow field. F_x: The force acting on the sample along the x-axis; F_y: The force acting on the sample along the y-axis. The gray band represents the trajectory of the negatively charged sample.

To proceed with the verification process, we must first establish and confirm several assumptions:

1. The flow velocity of the buffer and sample are identical upon entering the FFE zone.
2. The acceleration along the y-axis is solely influenced by the electric force, and the

duration of acceleration is negligible, allowing us to treat $\vec{v}_{sa,e}$ as a constant.

3. Similarly, it is assumed that the acceleration along the x-axis is solely governed by the drag force, and the acceleration time is also negligible. Consequently, $\vec{v}_{sa,f}$ follows a parabolic curve by laminar flow, which based on considering the channel to have a no-slip boundary.

To verify this assumption, consider a single particle in the sample. The particle owns the following characteristics:

$\mu_e = \ electrophoretic\ mobility = \frac{q}{6\pi r\eta}\ ({}^{m^2}/_{V.s})$

$q = the\ charge\ of\ the\ sample\ (C)$

$r = the\ ionic\ size\ of\ the\ sample\ (m)$

$m = the\ mass\ of\ the\ sample\ (kg)$

$\eta = the\ viscosity\ of\ the\ buffer\ ({}^{kg}/_{s\cdot m})$

$E = the\ applied\ electric\ field\ ({}^{V}/_{m})$

$V = the\ applied\ voltage\ (V)$

Along the y-axis, the laminar flow consistently exhibits zero velocity. Taking into account the drag force and electric force, we can establish the following relationship:

$$F_y = qE - 6\pi r\eta v_{sa,e}(t) = m\frac{dv_{sa,e}(t)}{dt} \qquad \text{(2-1)}$$

Solve it, we get:

$$v_{sa,e}(t) = \frac{qE}{6\pi r\eta}(1 - e^{-\frac{6\pi r\eta}{m}t}) \qquad \text{(2-2)}$$

Apply the real number in this equation ($r \approx 10^{-9}\ (m), m \approx 6.4\cdot 10^{-25}\ (kg), \eta \approx 10^{-3}\ (Pa\cdot s)$), we find that the exponential term can be neglect ($\approx e^{-10^{15}t}$). We get:

$$v_{sa,e}(t) = \mu_e \frac{V}{W_{ch}} \tag{2-3}$$

The expression remains constant, which indicates the fulfillment of assumption 2.

Now, let's consider force equilibrium along the x-axis, taking into account the parabolic flow pattern and the drag force. These considerations yield the following relationship:

$$\begin{cases} F_x = -6\pi r\eta(v_{sa,f}(t) - v_{flow}(t)) = m\dfrac{dv_{sa,f}(t)}{dt} & (2\text{-}4) \\ v_{flow}(t) = v_{flow,max}\left(1 - \dfrac{4}{W_{ch}^2}(y(t))^2\right) & (2\text{-}5) \\ y(t) = v_{sa,e}(t) \cdot t & (2\text{-}6) \end{cases}$$

where:

$v_{flow,max} = \ the\ maximum\ flow\ velocity = \frac{8Q}{\pi W_{ch}^2}({}^{mm}/_{s})$

$Q = volume\ flow\ rate\ ({}^{\mu L}/_{s})$

$W_{ch} = the\ width\ of\ the\ FFE\ channel\ (mm)$

In this context, v_{flow} represents the parabolic pattern resulting from the laminar flow, while $y(t) = v_{sa,e}t$ is applied in accordance with assumption 2. Now solve it, we get:

$$v_{sa,f}(t) = \left(Ce^{-\frac{6\pi r\eta}{m}t} + \frac{2v_{flow,max}v_{sa,e}^2 m}{3\pi\eta r W_{ch}^2}t + \frac{2v_{flow,max}v_{sa,e}^2 m^2}{9\pi^2 r^2\eta^2 W_{ch}^2}\right) + v_{flow,max}\left(1 - \frac{4v_{sa,e}^2}{W_{ch}^2}t^2\right) \tag{2-7}$$

Again, apply the real number in this equation ($r \approx 10^{-9}(m), m \approx 6.4 \cdot 10^{-25}(kg), \eta \approx 10^{-3}(Pa \cdot s)$), the first three terms can be neglected. We get:

$$v_{sa,f}(t) = v_{flow,max}\left(1 - \frac{4v_{sa,e}^2(t)}{W_{ch}^2}t^2\right) \tag{2-8}$$

This is same as the $v_{flow}(t)$, which suggests that regardless of the initial velocity

doi:10.6342/NTU202401456

of the sample, it will promptly conform to the parabolic curve, thus confirming the satisfaction of our assumptions 1 and 3.

After the assumption is confirmed, we can now analyze the sample motion. The sample velocity along x and y-axis can be written as following:

$$\begin{cases} \vec{v}_{sa,f}(t)\hat{\imath} = v_{flow,max}(1 - \dfrac{4v_{sa,e}^2(t)}{W_{ch}^2}t^2)\hat{\imath} & (2\text{-}9) \\ \vec{v}_{sa,e}(t)\hat{\jmath} = \mu_e \dfrac{V}{W_{ch}}\hat{\jmath} & (2\text{-}10) \end{cases}$$

Which is reference by the (2-3) and (2-8). Also, the trajectory equation can be denoted as:

$$\begin{cases} L_{ch} = \displaystyle\int_0^T \left|\vec{v}_{sa,f}(t)\right| dt & (2\text{-}11) \\ d = \left|\vec{v}_{sa,e}(t)\right| \cdot T & (2\text{-}12) \end{cases}$$

where:

$T = the\ time\ interval\ when\ sample\ travel\ from\ inlet\ to\ oulet\ (s)$

$L_{ch} = the\ length\ of\ the\ FFE\ channel\ (mm)$

$d = the\ deflection\ distance\ along\ y\ axis\ from\ inlet\ to\ outlet\ (mm)$

By (2-9) and (2-11), we can get:

$$L_{ch} = v_{flow,max}(T - \frac{4T^3 v_{sa,e}^2(t)}{3W_{ch}^2}) \tag{2-13}$$

Finally, by applying (2-10) and (2-12), the most interesting parameter, d can be denoted by the known variables:

$$L_{ch} = \frac{v_{flow,max} \cdot W_{ch}}{\mu_e V}(d - \frac{4d^3}{3W_{ch}^2}) \tag{2-14}$$

By utilizing equation (2-14), we can predict the motion of the sample by applying the known properties. This predictive capability enables us to optimize parameters such as chip dimensions or flow rate, leading to the achievement of the best FFE performance.

2.2 SERS theory

2.2.1 Principle of Raman scattering

Scattering is a fundamental physical phenomenon in which the interaction between light and matter causes changes in its direction, frequency, and intensity [132]. When energy is transferred from the photon to matter, it undergoes a rapid transition to a higher energy band, followed by the majority of molecules returning to the same energy band level. This phenomenon is known as Rayleigh scattering or elastic scattering. In the less likely scenario, there is a chance that the matter will either gain or lose energy, resulting in a higher or lower energy state than before. This process is referred to as Raman scattering, encompassing both Stokes and anti-Stokes scattering (Figure 2-2). Typically, the probability of Stokes scattering is significantly higher than that of anti-Stokes scattering, making Stokes scattering the primary focus of measurement. Raman scattering offers valuable insights into molecular structure, chemical composition, and other relevant properties. Through the analysis of frequency shifts and intensity changes in the scattered light, researchers can gather information about molecular vibrations, rotational modes, and electronic transitions within the sample [132]. However, traditional Raman scattering suffers from weak signal intensity, necessitating long acquisition times and high analyte concentrations to detect measurable signals. This limitation arises from the low probability of inelastic scattering events, where photons interact with molecular vibrations, leading to spectral shifts in the scattered light. To overcome this limitation, the emergence of surface-enhanced Raman scattering (SERS) has revolutionized the field by significantly enhancing the Raman signal, enabling highly sensitive detection and analysis.

doi:10.6342/NTU202401456

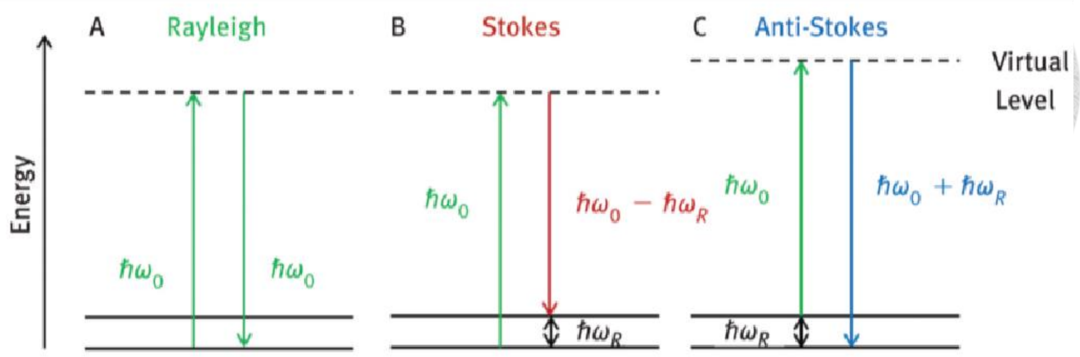

Figure 2-2 Schematic energy diagrams of various scattering [132].

2.2.2 Surface Enhancement Principle of SERS

SERS takes advantage of the unique properties of metallic nanostructures to enhance the Raman scattering signal. When molecules are adsorbed onto or close to these nanostructures, the localized surface plasmons generated on the metal surface interact with the incident laser light, resulting in a dramatic increase in the Raman signal. This enhancement arises from two mechanisms, including electromagnetic enhancement (EM) (Figure 2-3A), and chemical enhancement (CM) (Figure 2-3B).

Electromagnetic enhancement encompasses two main effects, namely local field enhancement and radiation enhancement. Local field enhancement occurs when the excitation wavelength is close to the optical resonance of the structures, known as localized surface plasmon resonances. This resonance results in the excitation of the Raman dipole and a subsequent enhancement, represented by the enhancement factor:

$$M_{Loc}(\omega_L) = \frac{|E(\omega_L)|^2}{|E_0(\omega_L)|^2} \tag{2-15}$$

where:

$\omega_L = The\ frequency\ at\ optical\ resonances\ of\ structures$

$M_{Loc} = Enhancement\ factor$

doi:10.6342/NTU202401456

$E_0(\omega_L) = The\ incident\ field$

This enhancement factor can reach values as high as 10^5, particularly for molecules located at hot spots.

Another crucial factor is radiation enhancement, resulting from the emission of the Raman dipole by the nearby metallic nanostructure. Combining these two effects yields the electromagnetic enhancement factor:

$$
\begin{aligned}
EF_{EM} &\approx M_{Loc}(\omega_L) * M_{Loc}(\omega_R) \\
&\approx \frac{|E(\omega_L)|^4}{|E_0(\omega_L)|^4}
\end{aligned}
\tag{2-16}
$$

where:

$\omega_R = The\ Raman\ frequency$

The results suggest that, in most situations, we can assume radiation and local enhancement have similar effects, leading to the approximation $|E|^4$ approximation. Consequently, the enhancement factor may reach up to the order of 10^{10} [133].

Chemical enhancement occurs as a result of changes in the electronic structure of molecules [134], typically resulting in an enhancement factor of around 10. Unlike electromagnetic enhancement, which alters the applied electric field, chemical enhancement (CM) influences molecular polarizability to enhance Raman scattering. The most extensively discussed theory in this context is known as the charge transfer mechanism. An illustration of this effect can be observed in the Figure 2-4. New electronic states arising from chemisorption act as resonant intermediate states in Raman scattering. This mechanism provides an alternative path for electrons to transition to a higher energy band, thereby intensifying the Raman shift.

doi:10.6342/NTU202401456

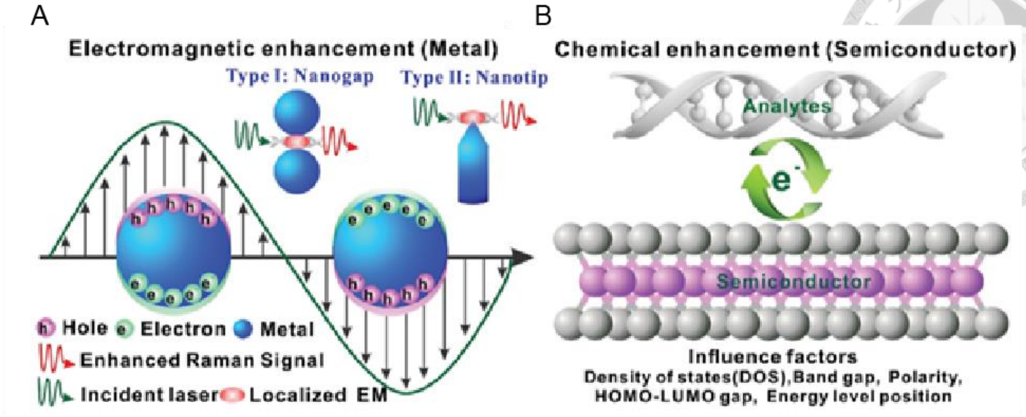

Figure 2-3 The Representative mechanisms of SERS [135]. (A) Electromagnetic enhancement. (B) Chemical enhancement.

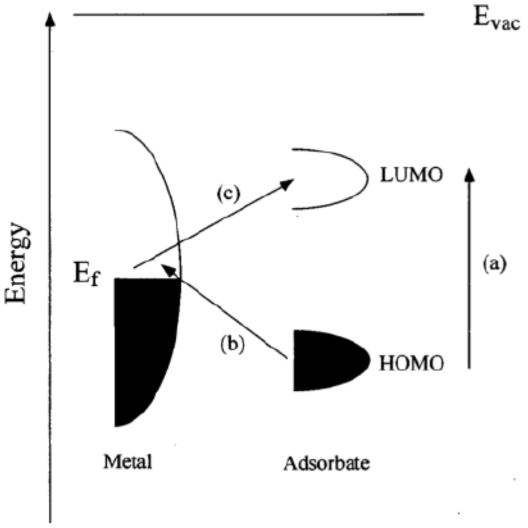

Figure 2-4 The illustration of the charge transfer mechanism [134].

2.3 Principal Component Analysis theory

Principal Component Analysis (PCA) aims to transform a high-dimensional dataset into a new coordinate system, highlighting the most significant patterns and structures within the data [136]. Figure 2-5 shows the whole process of the PCA [137]. The key idea is to identify principal components, which are linear combinations of the original variables capturing the maximum variance in the data. These components are orthogonal, ensuring they provide uncorrelated and independent information. PCA is a valuable tool with distinct advantages in dimensionality reduction, feature extraction, and data visualization. However, researchers must be cognizant of its limitations, particularly regarding linearity assumptions sensitivity, and Loss of Interpretability.

The PCA process involves the following steps: (1) Data standardization, (2) Selection of principal components, and (3) Data visualization [138]. Before applying PCA, it is essential to standardize the data by centering and scaling it. This step ensures that all variables contribute equally to the analysis, preventing dominance by variables with larger scales. Next, we need to find the principal components, which are the new coordinates allowing for the most variance in the data. The covariance matrix, based on standardized data, represents the relationships between different variables. The eigenvalues of this matrix represent the amount of variance captured by each principal component, while eigenvectors define the direction of these components in the original variable space. These components are then selected as the principal components, indicating that the number of principal components can be fewer than the number of variables, effectively reducing dimensionality. After finding the principal components, we can visualize the results. Typically, PCA results can be plotted in a scatter plot where the axes represent the first and second principal components (Figure 2-6A). The data points are grouped based on variance in these two principal components. To understand how much these two components explain the variance of the data, Proportion of Variance Explained (PVE) figures are often illustrated (Figure 2-6B). These figures show the cumulative variation for the number of principal components, allowing us to choose the appropriate number of principal components.

doi:10.6342/NTU202401456

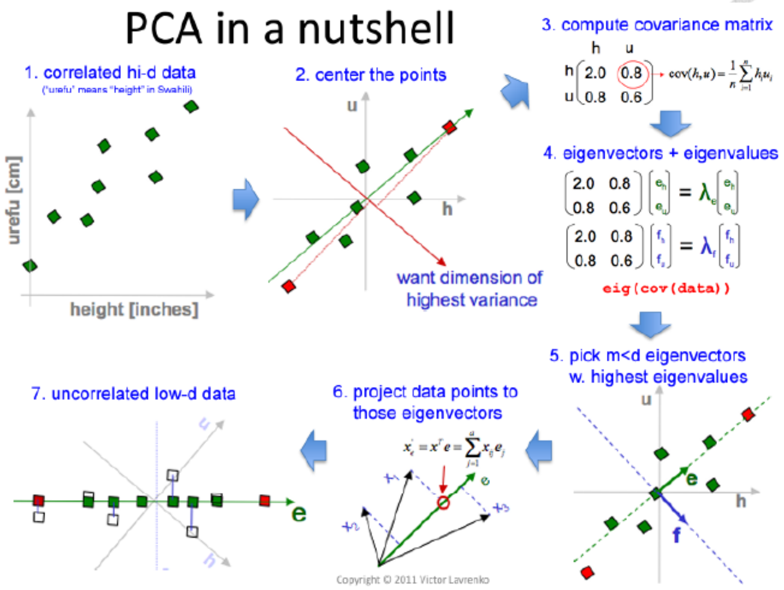

Figure 2-5 The schematic of the PCA process [137].

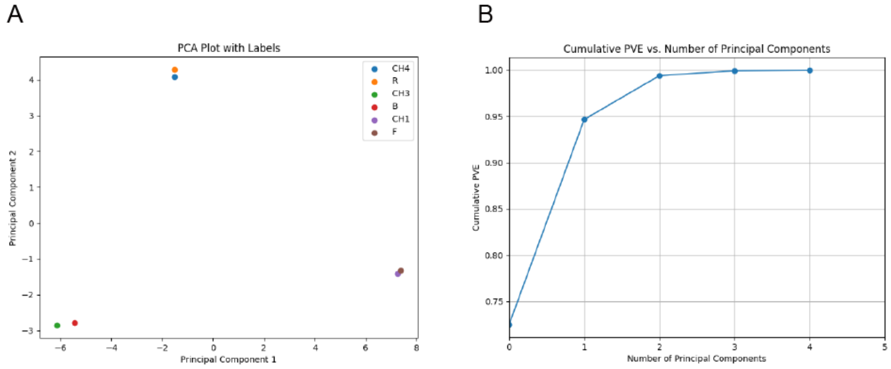

Figure 2-6 The example figure of the (A) PCA. (B) PVE.

Chapter 3 Materials and methods

In this section, we will provide a detailed overview of the experiments. Initially, we will introduce the entire system, encompassing both the μFFE and SERS regions. Subsequently, we will delve into the fabrication of the chip and outline the specific operational procedures for these systems. Next, the chemicals employed in the experiment will be discussed, followed by an explanation of the data processing methods.

3.1 System setup

3.1.1 System overview

A microfluidic system has been developed to integrate sample separation and optical detection into a single experimental setup. Figure 3-1A illustrates the entire process. Initially, the sample and buffer are loaded into the FFE region through the inlet, maintaining an optimized flow rate. Subsequently, an electric field is applied using the pre-set electrodes within the electrode channel to separate the sample based on different electric mobilities. The peristaltic pump then draws the liquid from the various outlets and directs it into the SERS detection zone. In the SERS detection region, Raman spectroscopy is employed, and the control platform generates a mapping laser spot for a detailed analysis of the sample.

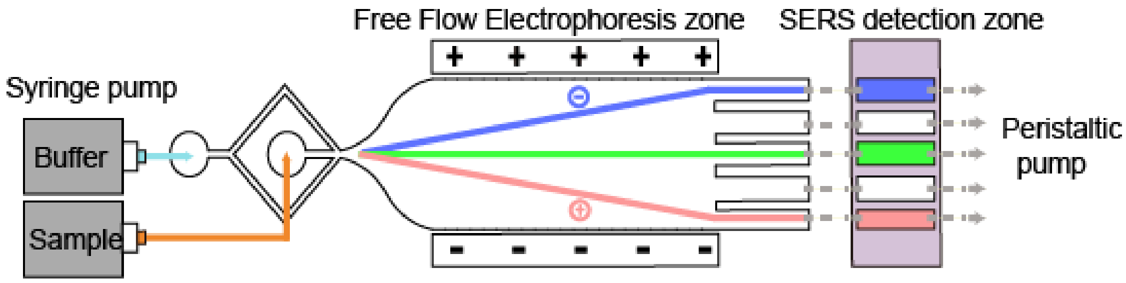

Figure 3-1 The schematic of the FFE-SERS system.

3.1.2 System design

The design of the PDMS channel for µFFE and SERS detection is depicted in Figure 3-2, with specific parameters outlined in Table 3-1. The chip size is tailored to accommodate a commercial glass cover, measuring 75 mm * 50 mm for the µFFE channel and 75 mm * 25 mm for the SERS channel. The main channel adopts a spindle shape instead of a diamond shape to prevent stagnant corners and enhance the flow pattern [139]. The Y-shaped channel inlet facilitates sheath flow generation for controlling analyte bandwidth [140]. Additionally, the barrier gap between the gel channel and the main channel is designed to prevent bubbles, serve as a gel-loading guide, and facilitate electrolyte transfer [28]. Figure 3-2C and Figure 3-2D display the bright-field image of the chip. The µFFE chip is primarily divided into three regions. Electrophoresis occurs in the main channel, with the gel channel serving as a barrier to prevent bubbles, and the electrode channel connected to the power supply to create the electric field. Additionally, for SERS detection, the PDMS channel is bonded to the SERS substrate and connected to the µFFE chip through Tygon tubes.

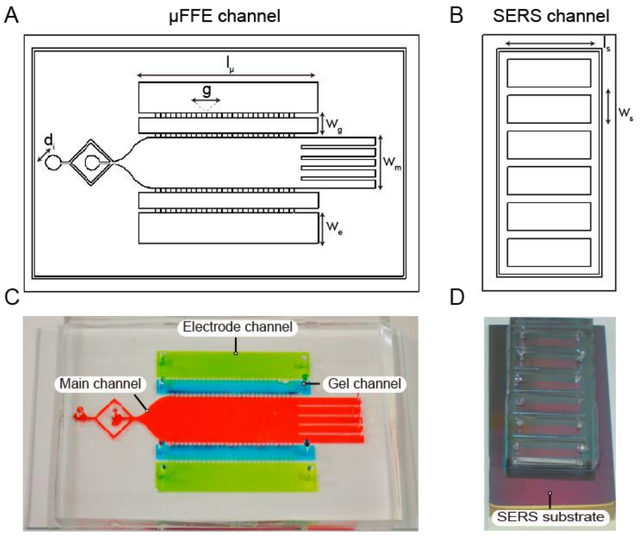

Figure 3-2 The design of the PDMS channel. (A) For µFFE (B) For SERS; The actual pictures of the PDMS chip. (C) µFFE (D) SERS.

Table 3-1 The microfluidic channel parameters.

μFFE channel	(mm)
Channel length (l_μ)	30
Main channel width (w_m)	10
Gel channel width (w_g)	3
Electrode channel width (w_e)	6
Inlet diameter (d_i)	3
Gap between Barrier (g)	0.1
Channel depth (d_c)	0.15
SERS channel	(mm)
Channel length (l_s)	15
Channel width (w_s)	5
Channel depth (d_s)	1

3.2 Fabrication protocols

3.2.1 Microfluidic chip fabrication

The microfluidic chip is manufactured through a two-step process: (1) PMMA mold fabrication and (2) PDMS channel fabrication. The whole process is shown in Figure 3-4. To create the microfluidic chip, the initial step involves designing a PMMA mold capable of producing micro-patterns using a Computer Numerical Control (CNC) machine. The 3D pattern is created using SOLIDWORKS 2019. In brief, a 2D sketch is drawn on a specific datum plane, and after determining the structure's parameters, the planar structure is extended to a 3D structure with the desired height. The resulting file is then converted into a CNC machine-readable format. Following this, a commercial PMMA plate will be

doi:10.6342/NTU202401456

fixed on the CNC machine (Figure 3-3B), with the surface pre-cleaned using an air gun and rinsed in ethanol for 15 minutes. The manufacturing process is set up with optimal parameters, such as the spin rate of the milling cutter or the path for the milling process. Finally, under the CNC control program, the designed pattern can be created within approximately four hours (Figure 3-3A).

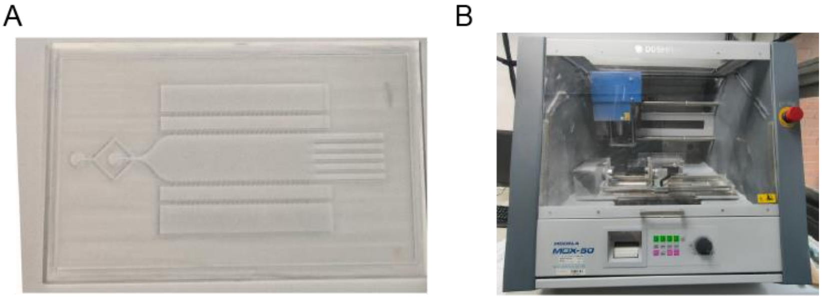

Figure 3-3 The actual picture related to the PMMA mold. (A) The processed PMMA mold. (B) CNC machine, which model is Roland MDX-50.

The subsequent step involves PDMS channel fabrication. We will pour the PDMS precursor, a mixture of elastomer and curing agent with a weight ratio of 10:1, onto the PMMA mold. After curing at 60°C for 4 hours, the PDMS structure can be peeled off from the mold. The following processes differ based on the function of the PDMS channel, whether it is intended for (1) μFFE or (2) SERS.

(1) For μFFE: The cured PDMS channel is initially punched using 1.5 mm, 0.3 mm, and 0.75 mm biopsy punches for the channel inlet, electrode, and channel outlet, respectively. Subsequently, the electrode channel is cut to eliminate the formation of electrolysis-generated bubbles. A 0.1 mm diameter platinum wire is then affixed to the pre-punched hole to establish a connection to the power supply. After a surface cleaning process using traceless tape, we apply O2 plasma (Plasma Cleaner PDC-001, Harrick Plasma) bonding with the commercial glass cover.

(2) For SERS: The cured PDMS channel is initially punched using 0.75 mm biopsy punches for the channel inlet and outlet. The surface is then cleaned using traceless tape. The subsequent bonding process involves a careful approach to prevent silver oxidation on the SERS substrate due to direct O2 plasma bonding, which could potentially affect the SERS measurement. To address this, we apply a PDMS coating as a glue between the PDMS channel and the SERS substrate. In this process, 5 mL of uncured PDMS mixture is poured into a 9 cm diameter petri dish and spun at 3000 rpm for 30 seconds. After spinning, a thin layer of liquid PDMS is obtained. The PDMS channel is gently placed in the petri dish and then directly positioned onto the SERS substrate. Following this, evacuation is performed to prevent the channel from contacting the air. The chip is subsequently placed in an oven at 60°C for 4 hours for further stabilization.

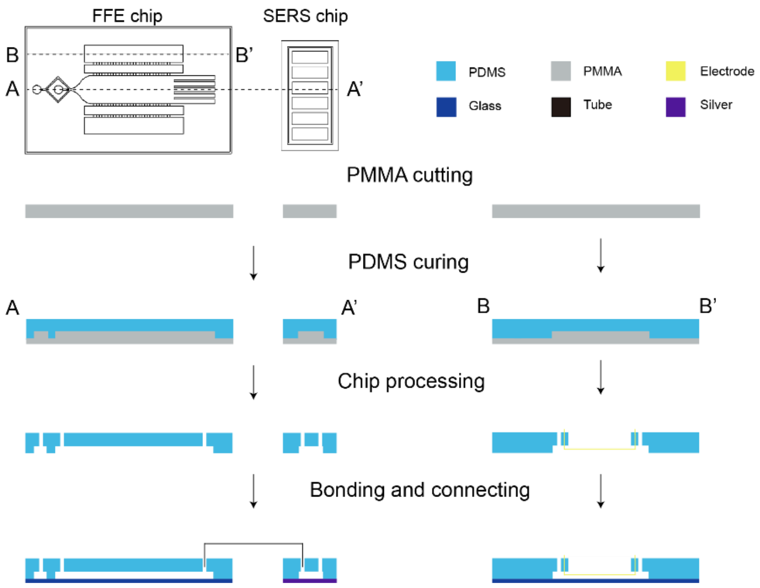

Figure 3-4 Schematic of the μFFE-SERS device fabrication procedure.

3.2.2 SERS substrate fabrication

The SERS substrate fabrication is done by Professor Yuh-Lin Wang's Lab, Institute of Atomic and Molecular Sciences, Academia Sinica, Taiwan [141]. The protocol for these 2D SERS substrates is outlined in Figure 3-5. In summary, the process begins with the fabrication of porous anodic aluminum oxide (AAO) by etching aluminum foil in 5% phosphoric acid, allowing for the fine-tuning of the gap between nanoparticles by controlling the etching time. Subsequently, silver is electrodeposited into these AAO holes, followed by etching the upper part of the AAO film to increase the exposed silver area (Figure 3-6).

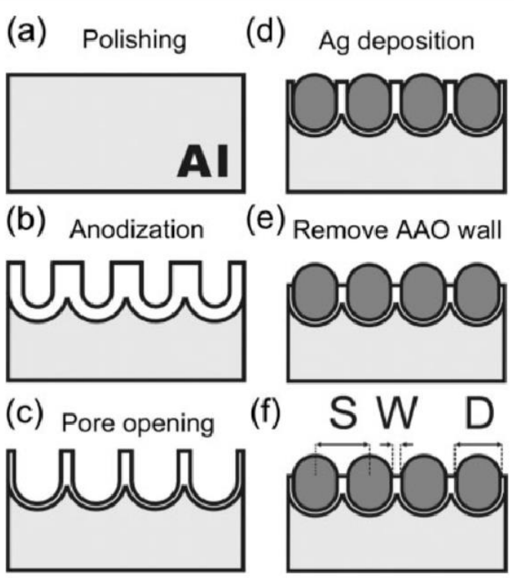

Figure 3-5 The schematic of the silver-filled AAO substrates [141].

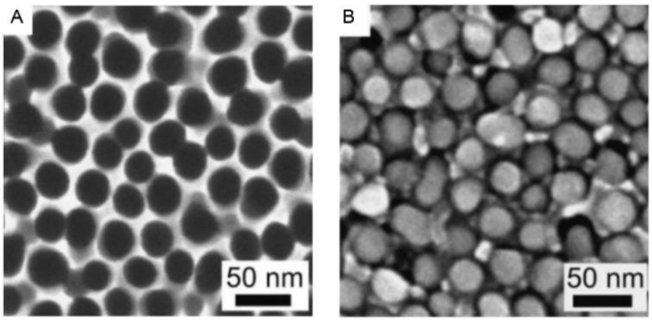

Figure 3-6 The SEM image of silver-filled AAO substrate. (A) before growth (B) after growth of silver nanoparticles [141].

doi:10.6342/NTU202401456

3.3 µFFE setup and process

The setup for the µFFE includes two syringe pumps (Nanojet pump, Chenyx) (SPLab02, Infusetek), one peristaltic pump (BT100-1L, LongerPump), and one power supply (MP-310, Major science). To initiate the FFE process, the µFFE chip undergoes a preprocessing step. The bonded µFFE chip is subjected to evacuation for 1 hour to create a microchannel under negative pressure, facilitating the easy filling of the entire channel with fluid. Following this, a liquid agarose gel (1% in 1X TAE) is injected into the gel channel through a pre-punched hole. The chip is then placed in a refrigerator at 4°C for 20 minutes for gel curing. Subsequently, the entire chip is filled with buffer to prevent bubbles.

Next, the chip is secured onto the microscope. Two syringe pumps are employed for injecting both the sample and buffer into the inlet. Simultaneously, a peristaltic pump extracts the sample from the outlet, while the power supply is connected to the electrodes embedded within the electrode channel. After the setup on the microscope, the buffer is initially injected into the channel for 10 minutes to ensure the stability of the flow system. Subsequently, the sample loading and application of the electric field are performed simultaneously to initiate the FFE. The separated sample from the outlet can then be used for fluorescence or SERS detection.

The whole process can be conducted on the Raman microscope, as depicted in Figure 3-7, the microscope stage enables the identification of the detection point, and automatic mapping can be performed after fixing the chip onto the microscope.

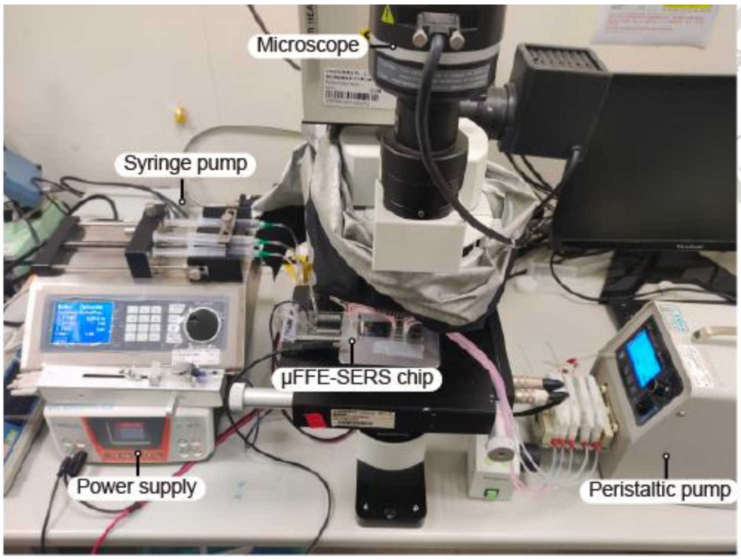

Figure 3-7 The experiment setup on the Raman microscope.

3.4 Optical setup

There are two types of optical setup: (1) Fluorescent microscope and (2) SERS microscope.

(1) Fluorescent microscope: The setup includes a CMOS camera (ORCA V3, Hamamatsu) mounted on the inverted microscope (OLYMPUS IX73) and an electrical control platform (Tango Desktop, Märzhäuser) controlled by OLYMPUS cellSens. For the experiment, a 2X objective (PlanN, Olympus) lens will be used. The exposure time is set at 75 ms. We have chosen the wide blue filter (Excitation: 460~495 nm; Emission: 510 nm up) to measure the fluorescent substance prepared in the experiment. The electrical platform enables video recording, image capturing, and long-range stitching.

(2) SERS microscope: The setup comprises an epi-fluorescent microscope (BX61WI, Olympus) equipped with a Raman fiber probe sensor (SuperHead HE 640, Horiba Jobin Yvon), CCD (354308, Horiba), He-Ne laser (632.8 nm, LGK 7665 P18,

LASOS), HE Raman spectrograph (HE633, Horiba), and an electrical motorized stage (EK32 75x50, Märzhäuser). For SERS detection, a 20× objective lens (MPlanFL N, Olympus) with a laser spot size of approximately 25 µm, and a laser irradiation power of 5 mW was chosen.

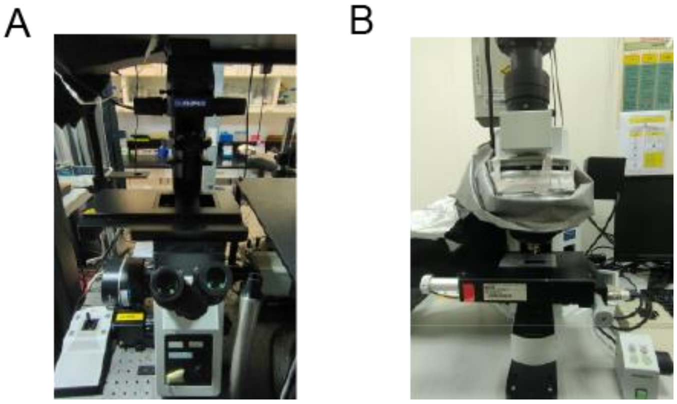

Figure 3-8 The actual picture of the (A) Inverted microscope. (B) Raman microscope.

3.5 Sample preparation

The reagents utilized in the experiment can be divided into three parts: (1) Buffer (2) Analytes (3) Support medium:

(1) Buffer: In the FFE experiment, the main channel buffer and the electrode channel buffer are maintained under the same conditions. Initially, 4-2-hydroxyethyl-1-piperazineethanesulfonic acid (HEPES) (Thermo Fisher) is selected as the fluorescent dye due to its suitable pH range [142], which is approximately 2.5~3.5 and 6.8~8.2. To optimize FFE performance, we set the condition at pH 7.5 by adjusting with sodium hydroxide (Thermo Fisher) and maintaining the concentration at 10 mM. Additionally, Sodium Acetic buffer, controlled at 0.05 M and pH 4, is used for the bacteria metabolites. Both solutions are stored at 25°C and protected from light.

(2) Analytes: Initially, we apply fluorescent materials, namely Rhodamine 6G, Rhodamine B, and fluorescein (Sigma-Aldrich), as proof-of-concept samples. The

doi:10.6342/NTU202401456

commercial solid matter is prepared in HEPES (pH 7.5, 10 mM, Sigma-Aldrich) and stored at 4°C. The stock solution is set at 1 mg/mL. Before the experiment, we dilute the solution with HEPES and add hydroxypropyl methylcellulose (HPMC) (0.2% w/w, Thermo Fisher) and Tween 20 (0.1% v/v, Thermo Fisher) as surfactants to prevent sample aggregation and adhesion on the surface [28]. Subsequently, the solution is shaken with a vortex mixer (Vortex Genie 2, Scientific Industries) for 5 minutes and filtered through a 3 μm membrane (Isopore Membrane Filter, Merck) to ensure the solution is well mixed and free of debris. Furthermore, bacteria metabolites and bacteria supernatants are prepared for biological applications. The bacteria metabolites, including adenine and uracil, are dissolved in acetic acid buffer at a concentration of 10-2 M and stored at 4°C.

(3) Support medium: The agarose gel (Thermo Fisher) is employed as a barrier to prevent bubble invasion from the electrode channel to the main channel. Initially, the solid agarose gel is dissolved to a concentration of 1% w/w in 1X Tris Acetate EDTA (TAE) (Thermo Fisher). It is then heated to over 90°C to transition the gel into the liquid phase. The liquid gel is stored in a 60°C oven to maintain it in the liquid phase.

3.6 Data analysis

The Origin 9 is used for data processing and visualization. The data processing procedure differs depending on the type of data obtained: (1) Fluorescence image and (2) SERS spectrum.

(1) Fluorescence image: First, the fluorescence and bright-field images of the chip are captured. These two images are set to the same size and location. A straight line is used to depict the location in proximity to the outlet, and the position of this line is

doi:10.6342/NTU202401456

recorded (Figure 3-9A). The same line is then applied to the fluorescence image, and the plot profile function in ImageJ is utilized to measure the fluorescence intensity along this line (Figure 3-9B). The intensity values range from 0 to 65535 for each pixel. Subsequently, the data are transferred to a TXT file and visualized through a line chart.

(2) SERS spectrum: Each SERS spectrum is averaged from three repeated measurements. For each sample, three SERS spectra are acquired to calculate the average and determine the error bar. Subsequently, the data undergo background removal using the sensitive nonlinear iterative peak clipping algorithm proposed by Miroslav's group [143]. The adjusted data are then transferred to Origin 9 for analysis and visualization. Additionally, these data undergo Principal Component Analysis (PCA) to confirm the separation efficiency.

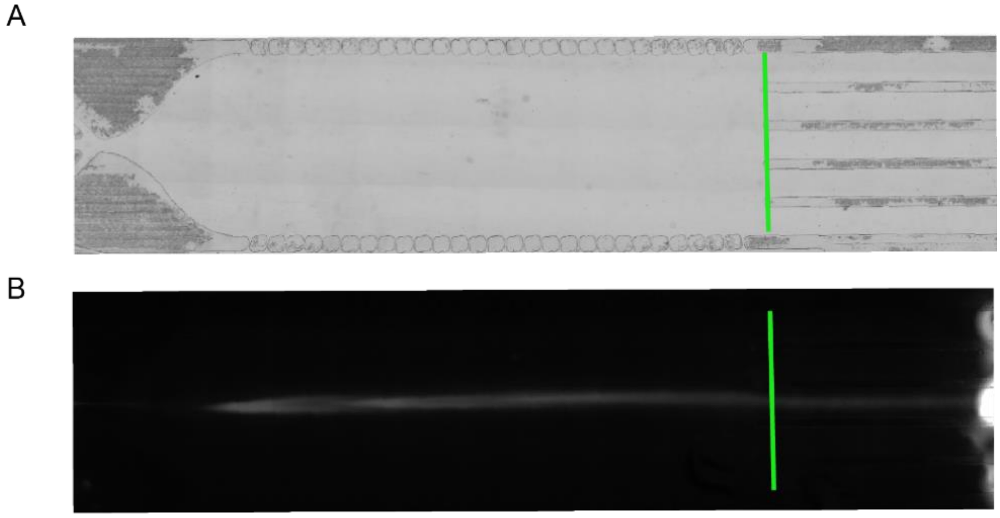

Figure 3-9 The example figures of the fluorescence image measurement under (A) bright field and (B) fluorescent field. The green line represents the measurement location.

3.7 Revised experimental protocol

To achieve better electrophoretic separation performance, we apply several

doi:10.6342/NTU202401456

modifications, including adjustments to the fabrication and µFFE setup and process, which are illustrated in Figure 3-10. Figure 3-11 shows the revised µFFE channel design, which includes a neck near the sample inlet to smooth the sample flow and reduce diffusion. Additionally, we design the radial outlet for easier manipulation. We also reduce the length, width, and depth of the channel, as shown in Table 3-2, to save mold space, lower sample consumption, and facilitate easier integration with the SERS detection system.

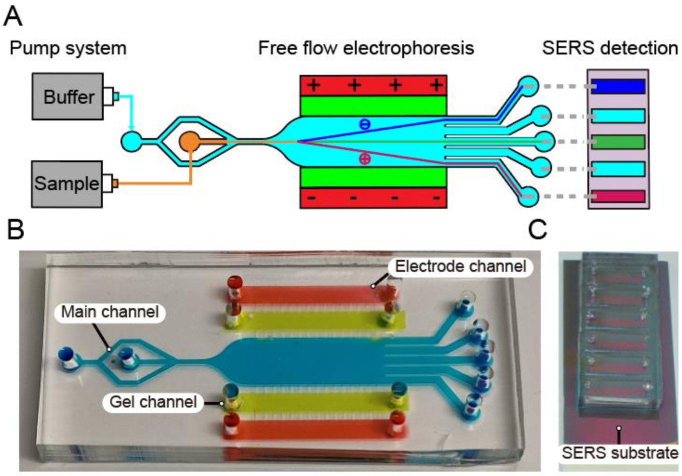

Figure 3-10 (A) The schematic of the revised FFE-SERS system. The actual pictures of the PDMS chip. (B) µFFE (C) SERS.

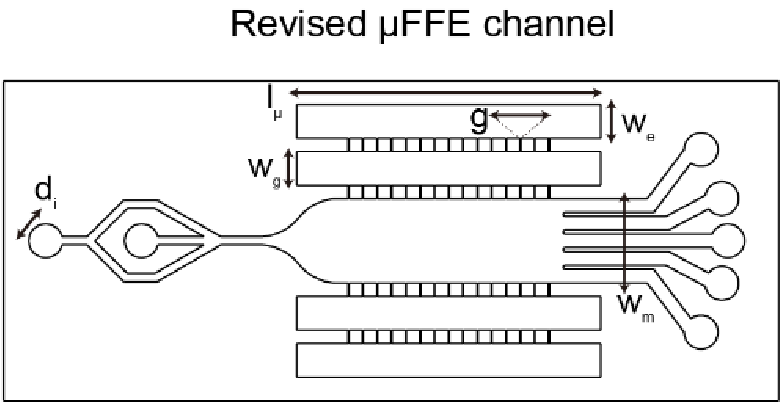

Figure 3-11 The revised design of the PDMS channel for µFFE.

doi:10.6342/NTU202401456

Table 3-2 The microfluidic channel parameters for the new design.

μFFE channel	(mm)
Channel length (l_μ)	15
Main channel width (w_m)	5
Gel channel width (w_g)	2
Electrode channel width (w_e)	2
Inlet diameter (d_i)	2
Gap between Barrier (g)	0.05
Channel depth (d_c)	0.1

3.7.1 Revised microfluidic chip fabrication

Except for the PMMA molding, we aim to utilize silicon molds fabricated through photolithography processes (Figure 3-12). This approach offers several advantages, including more stable flow patterns, the ability to achieve lower channel heights for improved FFE performance, and increased efficiency in chip production. The MICRO CHEM SU-8 2050 negative photoresist is used to fabricate the 100 μm height channel. The brief process is illustrated as follows:

(1) Wafer cleaning: The wafer is washed with CH_3COCH_3 to remove particles and a mixture of H_2SO_4 and H_2O_2 to break the hydrocarbon bonding of organic compounds. Buffered oxide etching (BOE) is used to remove the thin oxide layer. DI water rinsing is performed between these steps. Finally, the wafer is dried with an N2 gun and placed in a 120℃ oven for 10 minutes.

(2) Spin-coating: Then the negative photoresist is poured onto the wafer and spun using

a spin coater to form a uniform thin film, which determines the thickness of the photoresist. Initially, the wafer is spun at 500 rpm for 10 seconds, followed by 1000 rpm for 10 seconds, and finally at 1750 rpm for 35 seconds.

(3) Soft bake: To improve the adhesion of the resist to the substrate, evaporate the remaining solvent in the photoresist by heating at 95°C for 5 minutes.

(4) Exposure and Post-exposure bake: The wafer is then placed on the photolithography system. Exposure to light causes a chemical change that allows the developer to remove unexposed regions of the negative photoresist. The wafer is then baked at 95°C for 9 minutes to promote diffusion, which rearranges the photoresist structure.

(5) Development: Finally, the wafer is rinsed with isopropanol to emerge the profile.

After the photolithography process is completed, the cured PDMS channel is initially punched using 2.5 mm and 1.5 mm biopsy punches for the channel outlet and other openings, respectively. Following a surface cleaning process with traceless tape, we apply O_2 plasma (Plasma Cleaner PDC-001, Harrick Plasma) to bond the PDMS channel with a commercial glass cover.

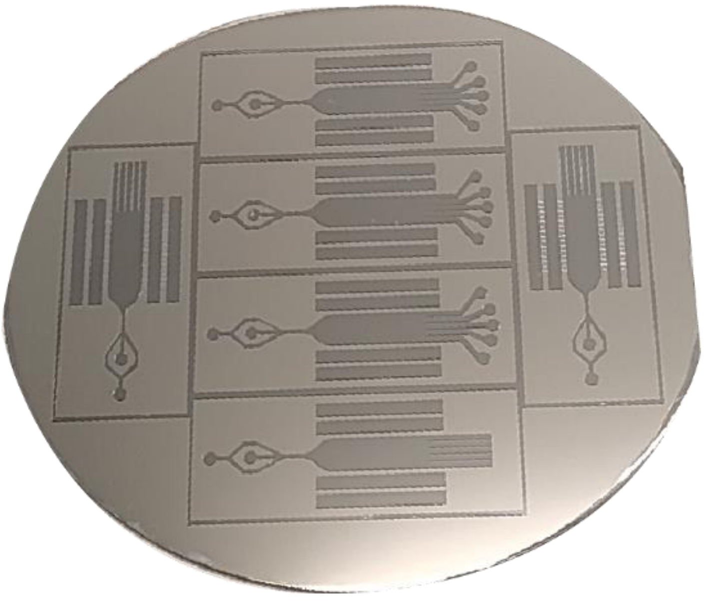

Figure 3-12 The image of the fabricated mold.

doi:10.6342/NTU202401456

3.7.2 Revised μFFE setup

Although we initially use a platinum electrode to apply the electric field, certain limitations such as the complicated chip fabrication process or issues with bubbles may interfere with the system's performance. Here, we replace the platinum electrode with a liquid electrode, which has the advantage of easy incorporation into the microfluidic system and fewer issues with bubbles. We use 3M KCL as the liquid electrode, eliminating the need for the electrode integration process mentioned in 3.2.1.

Chapter 4 Results and discussion

4.1 Simulation results

To optimize the parameters of the FFE, a finite element analysis was performed using COMSOL simulation. In section 4.1.1, the sheath flow effect was verified concerning different buffer and sample flow rate ratios. Moving on to section 4.1.2, the optimal flow rate for the FFE was determined. In this section, the simulation was still based on the theory that we had verified in section 2-1 but additionally considered convection and diffusion, which influenced the sample concentration from the outlet. The important parameters applied in the simulation are shown in Table 4-1. The "Laminar flow," "Electrostatics," and "Transport of Diluted Species" modules were applied for the simulation, and the geometry was based on the actual chip dimensions (Figure 3-2). The obtained results were then applied to the experiment.

Table 4-1 The parameters for COMSOL simulation.

Electrophoretic mobility	(m^2/V*s)
R6G [144]	$1*10^{-8}$
Rhodamine B	0
Fluorescein [144]	$-2*10^{-8}$
Diffusion coefficient	(m^2/s)
R6G [145]	$4*10^{-10}$
Rhodamine B [145]	$4.2*10^{-10}$
Fluorescein [146]	$6.4*10^{-10}$

4.1.1 Sheath flow ratio verification

The generation of sheath flow was crucial for the resolution of FFE, as it ensured the

doi:10.6342/NTU202401456

collection of the sample into the same outlet channel. In this scenario, we applied sheath flow with various buffer flow rates while maintaining a constant sample rate. No voltage was applied to solely consider the effects of sheath flow, convection, and diffusion. The initial sample concentration was set at 0.5 mol/m³. The results are depicted in Figure 4-1 (A). When the $Q_b : Q_s$ ratio is 20, the sample fails to concentrate into a specific outlet channel, resulting in insufficient separation and dilution. When the ratio reached 40, although the band became narrow enough, the concentration was diluted to 0.05 mol/m³, almost 1/10 of the initial concentration. Considering both bandwidth and concentration, we ultimately selected a ratio of 30, which provided good separation efficiency and controlled the outlet concentration to 1/5 of the initial concentration. Additionally, we calculated the Péclet number:

$$P_e = \frac{L \cdot \mu}{D} \tag{4-1}$$

where:

$L = characteristic\ length$ (m)

$\mu = local\ flow\ velocity$ (m/s)

$D = mass\ diffusion\ coefficient$ (m^2/s)

In our simulation conditions, we applied $L = 3 \cdot 10^{-2}\ (m), \mu = 6.6 \cdot 10^{-4}\ (\mathrm{m/s}), D = 10^{-10}\ (\mathrm{m}^2/\mathrm{s})$, result that $P_e \gg 1$. This demonstrated that the dilution of the sample was primarily influenced by convection rather than diffusion.

doi:10.6342/NTU202401456

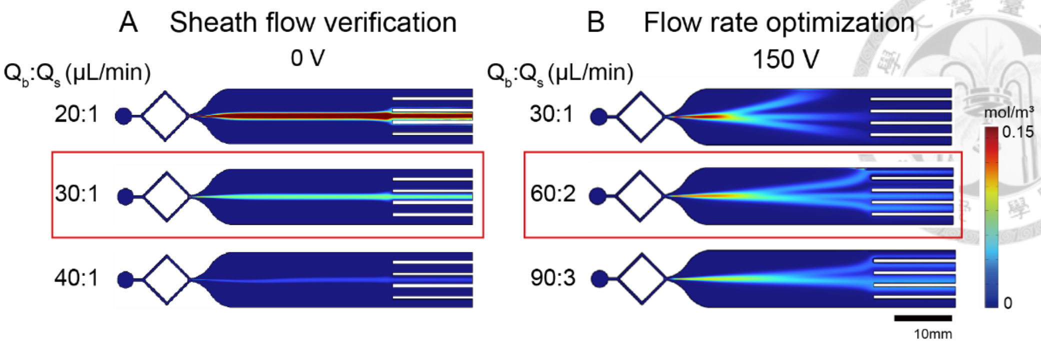

Figure 4-1 The COMSOL result of the sample concentration under different ratios of buffer and sample flow. (A) Sheath flow verification. (B) Flow rate optimization. Q_b: flow rate of buffer. Q_s: flow rate of the sample.

4.1.2 Flow rate optimization

After confirming the optimal sheath flow ratio, our subsequent step involved using COMSOL simulation to determine the ideal flow rate for conducting Free Flow Electrophoresis (FFE). The applied voltage was held constant at a stable 150 V, representing the maximum voltage that ensured system stability. Three sets of parameters were employed in the analysis, each maintaining the same ratio between Q_b and Q_s. The simulation results, presented in Figure 4-1 (B), indicated that if the flow rate was too high, the residence time in the electric field was insufficient for effective sample separation. Conversely, if the flow was too low, the separated band might adhere to the channel wall or even intrude into the gel channel, thereby compromising separation efficiency. Our analysis revealed that Q_b = 60 μL/min and Q_s = 2 μL/min yielded the optimal FFE performance, successfully separating the majority of the sample into different outlet channels. This parameter was employed in subsequent experiments. Additionally, we simulated the pressure field and flow velocity field at the optimal flow rate, and the results are shown in Figure 4-2. In summary, the pressure field was symmetric and stable for our experiment, with the maximum pressure occurring at the inlet channel, which was still suitable (approximately 5 Pa) for microfluidic experiments. The simulation also indicated that since the buffer flow rate was 30 times that of the sample flow rate, the flow velocity was primarily dependent on the buffer flow, resulting in a maximum of 0.66 mm/s in the main channel.

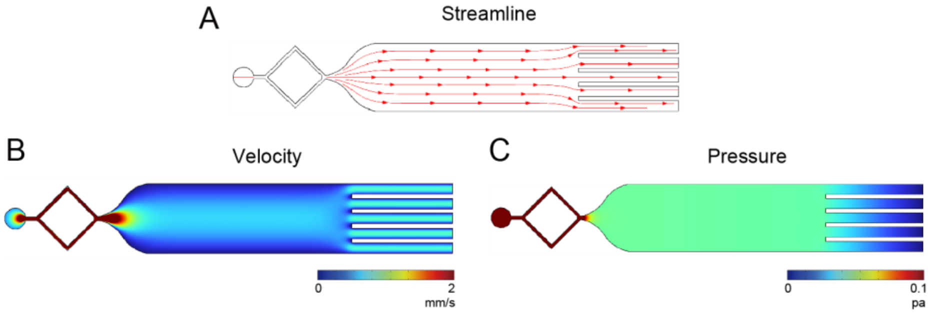

Figure 4-2 The COMSOL result of the surface plot for (A) streamline (B) velocity (C) pressure under $Q_b : Q_s = 60 : 2$ μL/min situation.

4.2 Sample characterization and optimization

In this chapter, the single sample FFE was performed to quantify the separation result. Additionally, the SERS signal calibration curve of the sample was conducted to verify the SERS chip performance.

4.2.1 Single sample FFE result

We applied a single sample to demonstrate the manipulation of the sample band into different outlet channels under varying flow rates and applied electric fields. The flow rate followed the simulation result, which was $Q_b = 60$ μL/min, $Q_s = 2$ μL/min. The residence time, which denotes the time the sample spent in the FFE region, can be estimated using (2-9) and (2-11), resulting in approximately 45 seconds. Considering this residence time, we waited for one minute after performing FFE to capture the fluorescent picture.

Figure 4-3 displayed the fluorescent images of different samples under three

doi:10.6342/NTU202401456

assigned voltages and the corresponding intensity diagrams measured from the starting side of the outlet. The zero position represented the center of the third outlet. The results showed that the charged sample deflected more as the applied voltage increased. For fluorescein, we observed it deflecting to the first channel when applying 150 V, while R6G deflected to the fourth channel under the same voltage, demonstrating that the simulation was suitable for real experiments. It is worth mentioning that the results indicated some samples deviated towards different outlets, primarily due to an imbalanced flow pattern near the outlets at 75 V for fluorescein or R6G. This test provided conclusive evidence of our ability to manipulate samples through the application of an electric field.

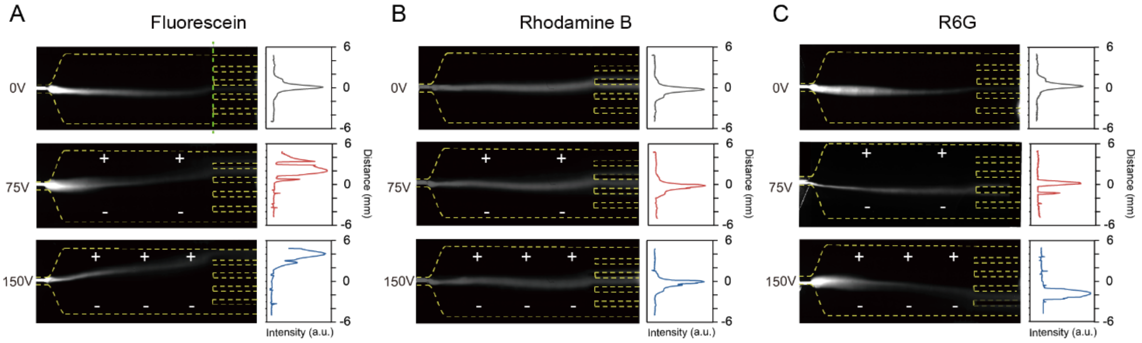

Figure 4-3 The μFFE result and intensity diagram of (A) Fluorescein (B) Rhodamine B (C) R6G. The green line represents the measured coordinate.

4.2.2 SERS calibration curves

To demonstrate the quantification property of the SERS substrate, the concentration calibration of the fluorescent dye was performed. Under the same optical parameters, such as exposure time or lens magnification, various concentration samples (ranging from 1 μg/mL to 1 mg/mL) were applied for calibration. Nine data points were acquired and averaged for further analysis. We choose a laser integration time of 1s. To better identify the correlation of each SERS spectrum, the characteristic SERS spectrum was normalized between 1200 cm^{-1} and 1600 cm^{-1}. Four-parameter logistic regression was employed to generate the calibration curve, which showed the R-squared values of 0.9824 (fluorescein), 0.9946 (rhodamine B), and 0.9887 (R6G). The results are shown in Figure 4-4. In conclusion, the limits of detection are 1.9 μg/mL for fluorescein, 2.4 μg/mL for rhodamine B, and 1.1 μg/mL for R6G. With these calibration curves, we can quantify the sample concentration after performing the FFE.

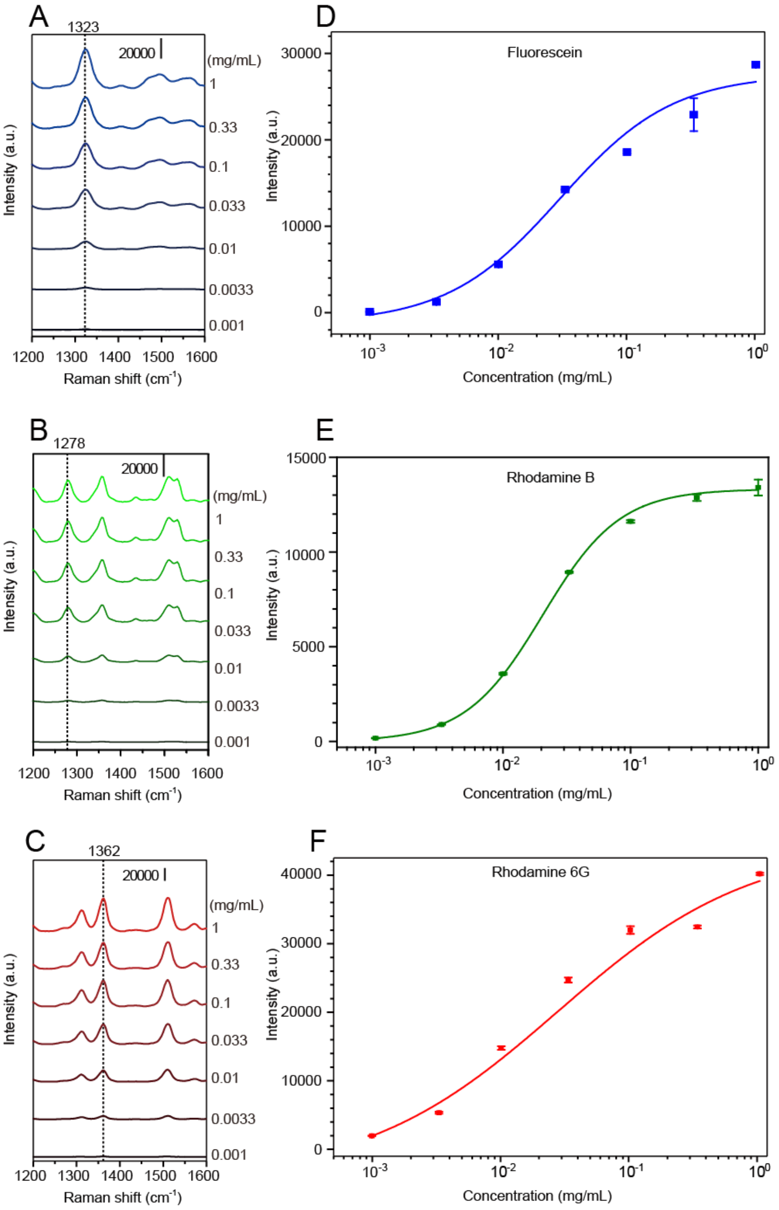

Figure 4-4 The SERS spectrum of fluorescent dye. (A) Fluorescein. (B) Rhodamine B. (C) Rhodamine 6G. The standard curve of (D) Fluorescein. (E) Rhodamine B. (F)

Rhodamine 6G. The dashed line represents the peak value for calibration.

4.3 Preliminary results

Since we had already demonstrated FFE manipulation and SERS calibration, we aimed to integrate these two techniques for the online FFE-SERS experiment (Figure 3-7) involving rhodamine B, R6G, and fluorescein. The entire FFE process took approximately three minutes, with a 30-second image capture period. Additionally, SERS detection took about ten minutes, highlighting the efficiency of FFE-SERS, which could be completed in less than fifteen minutes. As a proof of concept, we applied 1 mg/mL as the initial concentration for these samples and determined their concentration in the outlet using the calibration curve. The fluorescent image result is shown in Figure 4-5A and Figure 4-5B. This result corresponded to the simulation result (Figure 4-1B), which shows that the smaller electrophoretic mobility sample (R6G) will deflect less than the higher one (Fluorescein). The figure also reveals some discontinuities in the sample bands, attributed to the pulsations generated by the peristaltic pump. The SERS spectra are showcased, and we conducted a comparative analysis with standard SERS spectra. Further analysis was performed using principal component analysis (PCA). The differences between the data were analyzed by PC1 and PC2, accounting for 94.5% and 4.6%, respectively, and totaling 99.1% of the total differences. This indicates a high degree of spectrum correlation, affirming that the FFE-SERS system can be employed for multiplex biomolecular analysis. Also, since we verified the purity of the separated sample in the outlet, it was suitable to estimate the sample concentration, which was 0.11, 0.15, and 0.13 mg/mL for fluorescein, rhodamine B, and R6G, respectively.

doi:10.6342/NTU202401456

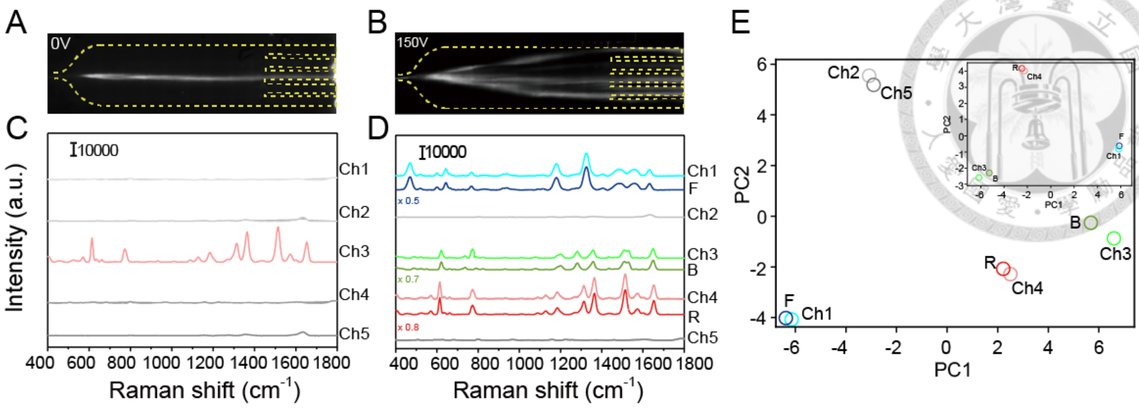

Figure 4-5 The proof-of-concept result for three fluorescent dyes flowed into the FFE-SERS system. The fluorescent image under (A) 0 V. (B) 150 V. The SERS spectrum under (C) 0 V (D) 150 V. (E) PCA result of the SERS spectrum from five outlets of the FFE channel under 150 V.

4.4 Biomolecule FFE-SERS demonstration

4.4.1 Mixing purine derivative quantification

In this section, our goal was to separate the mixture of adenine and uracil, the main metabolites secreted by bacteria, with varying concentrations. To quantify the concentration, we initially conducted a concentration calibration. We chose a concentration range from 10^{-4} M to 10^{-8} M for both adenine and uracil, acquiring nine data points that were averaged for further analysis (Figure 4-6). We utilized a laser integration time of 1s. For improved correlation analysis of each SERS spectrum, the characteristic SERS spectrum was normalized between 700 cm^{-1} and 900 cm^{-1}. We employed a four-parameter logistic regression to generate the calibration curve, revealing R-squared values of 0.984 (adenine) and 0.992 (uracil). In conclusion, the limits of detection were determined to be $8.4*10^{-8}$ M for adenine and $9.7*10^{-7}$ M for uracil. Following calibration, we conducted mixing sample FFE with $5*10^{-6}$ M: $5*10^{-5}$ M ratios

doi:10.6342/NTU202401456

of adenine compared to uracil.

The FFE results are shown in the Figure 4-7A and Figure 4-7B. It was observed that uracil remained neutral when subjected to 150 V, while adenine exhibited positively charged properties. This finding aligned with a study that reported the pKa of adenine as 4.2 and uracil as 9.4 [147,148]. When the pH exceeded the substance's pKa, protonation occurred; however, for uracil, the protonated form remained neutral. By adjusting the pH value of the buffer to pH = 4, we successfully separated samples with different electric properties. The intensity comparison results were depicted in Figure 4-7C and Figure 4-7D. Initially, the intensity under the LOD appeared to be zero, confirming our ability to deflect the sample into a specific channel regardless of applied voltage; for instance, adenine deflected to outlet 4, and uracil remained at outlet 3. Subsequently, the concentrations in the outlets were determined. Using the calibration curve, we found that the concentrations of adenine in outlet 4 and uracil in outlet 3 under 150 V were approximately 3.3*10-7 M and 4.1*10-6 M, respectively, resulting in a dilution factor of about 1/12. This dilution factor was slightly larger than the estimated factor, which assumed that the entire sample flow would go to a single outlet, while the buffer flow would be distributed evenly among the five outlets, resulting in a dilution factor of 1/7 (calculated as 2/ (2+60/5)). The possible reasons for the discrepancy may have included uneven buffer flow in the five channels or the sample deflecting into multiple channels. Despite the influence of apparatus limitations and substrate uniformity on the quantification of the SERS signal, our results demonstrated our ability to estimate sample concentrations.

doi:10.6342/NTU202401456

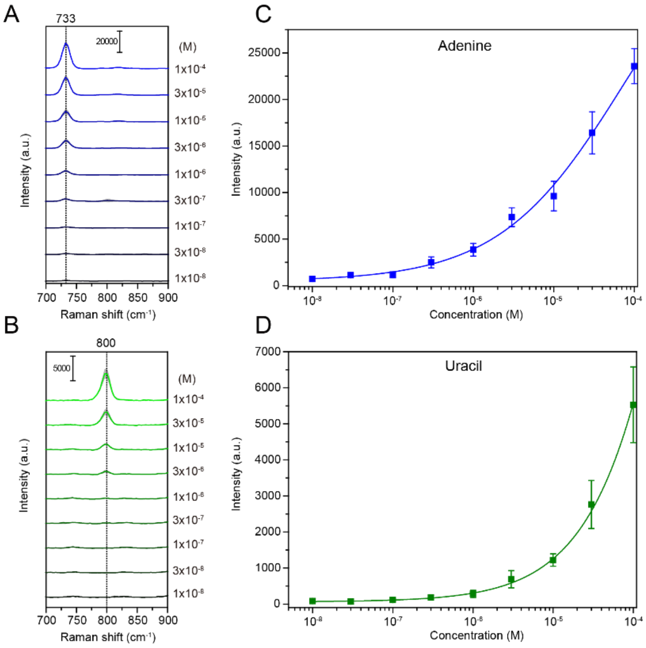

Figure 4-6 The SERS spectrum of purine derivatives. (A) Adenine. (B) Uracil. The standard curve of (C) Adenine. (D) Uracil. The dashed line represents the peak value for calibration.

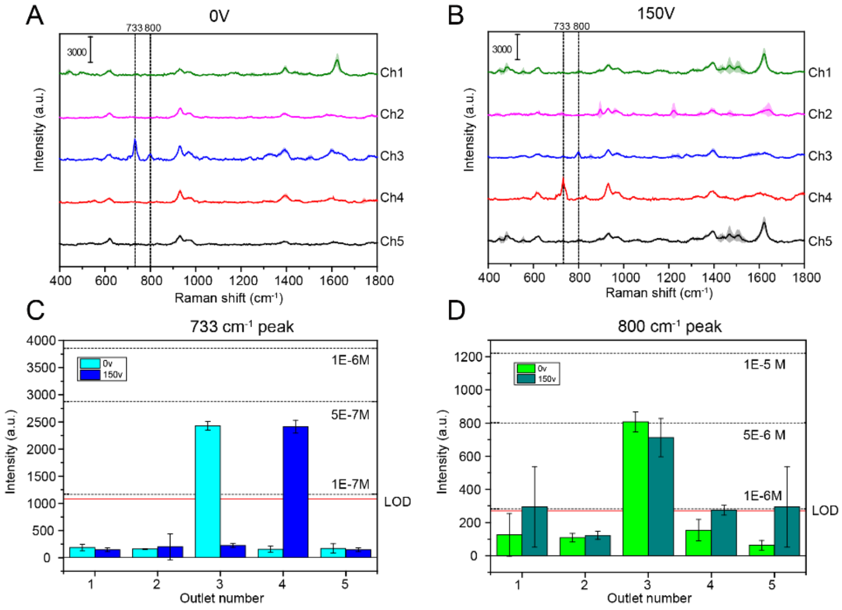

Figure 4-7 The FFE results for purine mixing under (A) 0 V and (B) 150 V; The comparison of peak intensities at Raman shifts of (C) 733 cm^{-1} (D) 800 cm^{-1} between 0 V and 150 V.

4.5 Results of the revised experimental protocol

In this section, we presented the results of fluorescence sample and purine mixing separation using the revised experimental protocol to demonstrate that our new design effectively achieved sample analysis while reducing system complexity, increasing fabrication efficiency, and lowering power consumption. First, we evaluate the sample/buffer flow rate ratio, which will cause the sheath flow wider or narrower, we apply three ratios, 20 : 1, 40 : 1 and 60 : 1, Figure 4-8B shows that when the $Q_b : Q_s$ ratio is 20, the sample failed to concentrate into a specific outlet channel, resulting in insufficient separation and dilution. Although the band became narrow enough, when the ratio is over 40, too high a ratio may result in the over-dilution of the sample, which is negative for the detection. Considering both bandwidth and concentration, we ultimately selected a ratio of 40, which provided good separation efficiency and controlled the moderate sample concentration.

After that, we aim to determine the ideal applied voltage for conducting FFE. We choose $Q_b : Q_s = 20 : 0.5$ µL/min to meet the validated ratio and because this flow rate is the lower bound for syringe pump stability, which also minimizes sample and power consumption. Figure 4-8C shows the COMSOL simulation results for different applied voltages. At an applied voltage of 24 V, we successfully separate the different fluorescent samples into different outlets.

doi:10.6342/NTU202401456

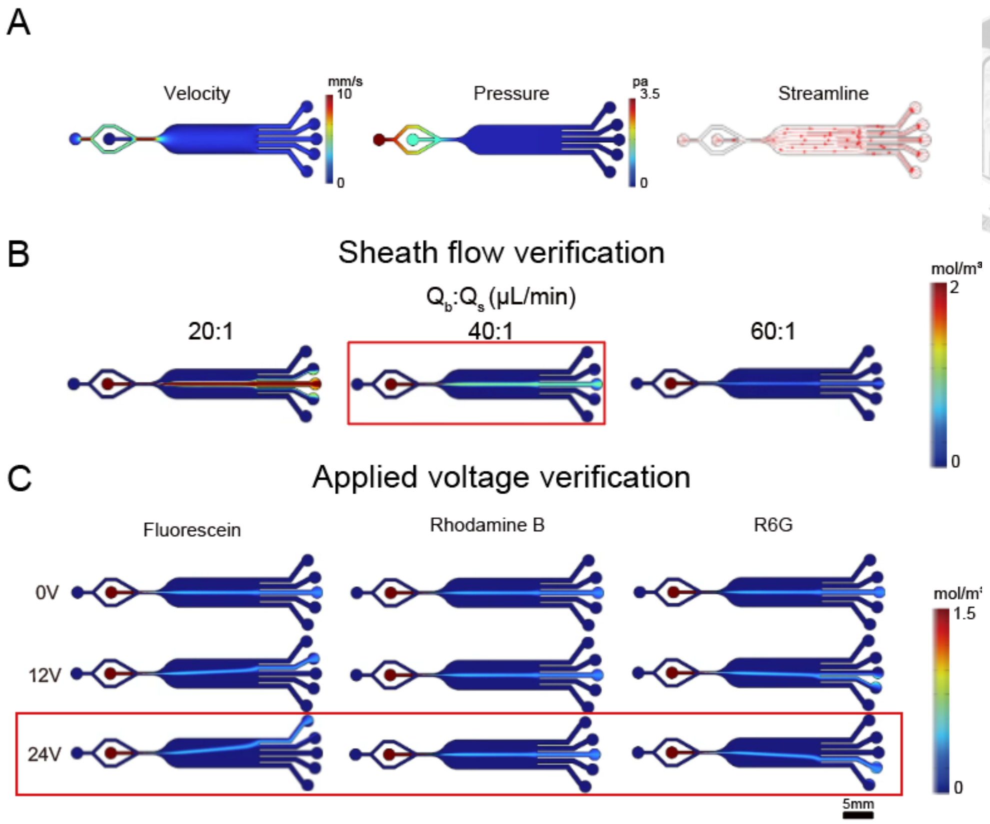

Figure 4-8 The COMSOL result of the sample concentration for (A) Microfluidic stability verification. (B) Sheath flow verification (C) Flow rate optimization. Q_b: flow rate of buffer. Q_s: flow rate of the sample. The red square represents the chosen parameter.

After optimizing the best flow rate and applied voltage, we conducted experiments to verify the performance. Figure 4-9 shows the result of single sample separation. Although we halved the channel width and length (comparing parameters in Table 3-1 and Table 3-2), we still successfully manipulated the sample into the target outlet. The discontinuity of the sample band occurred due to the limitations of the syringe pump. While increasing the flow rate could have addressed this issue, the primary intention of this experiment was to demonstrate system operability while saving sample demand and power consumption. Therefore, we used this parameter to perform the following experiments.

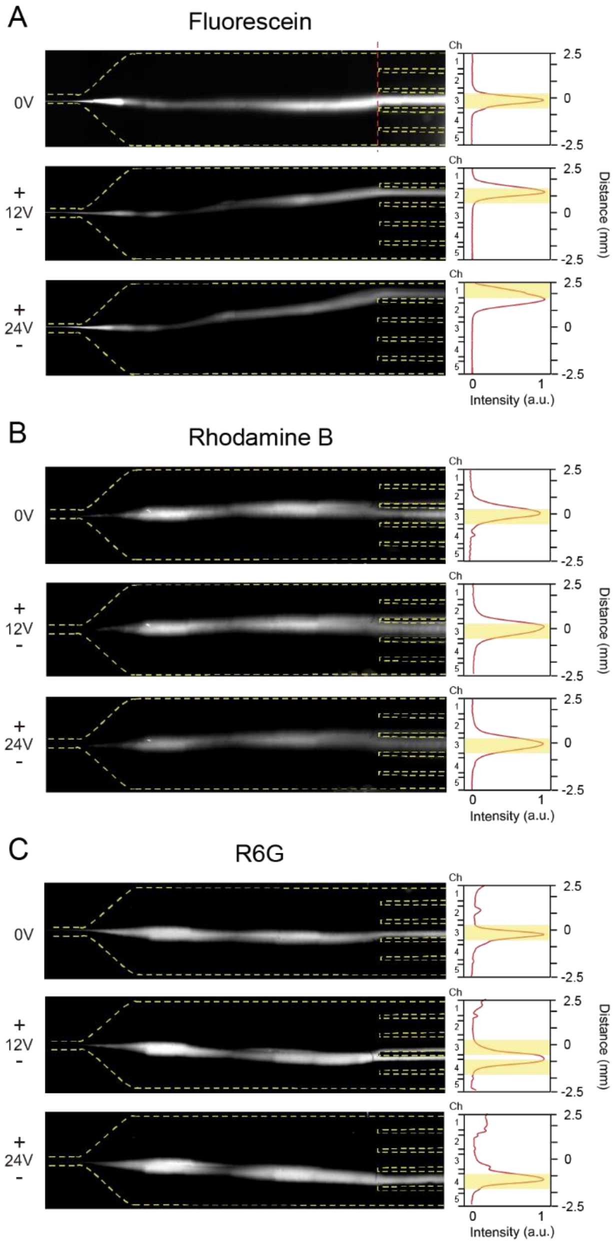

Figure 4-9 The μFFE result and intensity diagram of (A) Fluorescein (B) Rhodamine B (C) R6G. The green line represents the measured coordinate.

Figure 4-10 shows the results of the fluorescent mixing separation. Since the channel dimensions were reduced by half compared to the previous design, the separated sample bands came closer together, which could cause the separated samples to re-mix and affect the detection results. However, as seen in Figure 4-10C, Figure 4-10D, and Figure 4-10E, the mixed samples are still separated into distinct SERS spectra and could be grouped with the stock solutions of these samples in the PCA plot. Finally, we demonstrate the biological application by separating adenine and uric acid under pH = 7.5 conditions, according to the Benn, C. L. *et al*, uric acid will become negative charge when in the human body condition [149], so here we choose the adenine and uric acid to separate in the pH = 7.5. The calibration curve for uric acid, ranging from 1E-4 M to 1E-8 M, is shown in Figure 4-11, with the 1130 cm^{-1} peak used as the reference. Following the previous experimental protocol. The separation results, shown in Figure 4-12, indicated the successful separation of these two common bacterial metabolites.

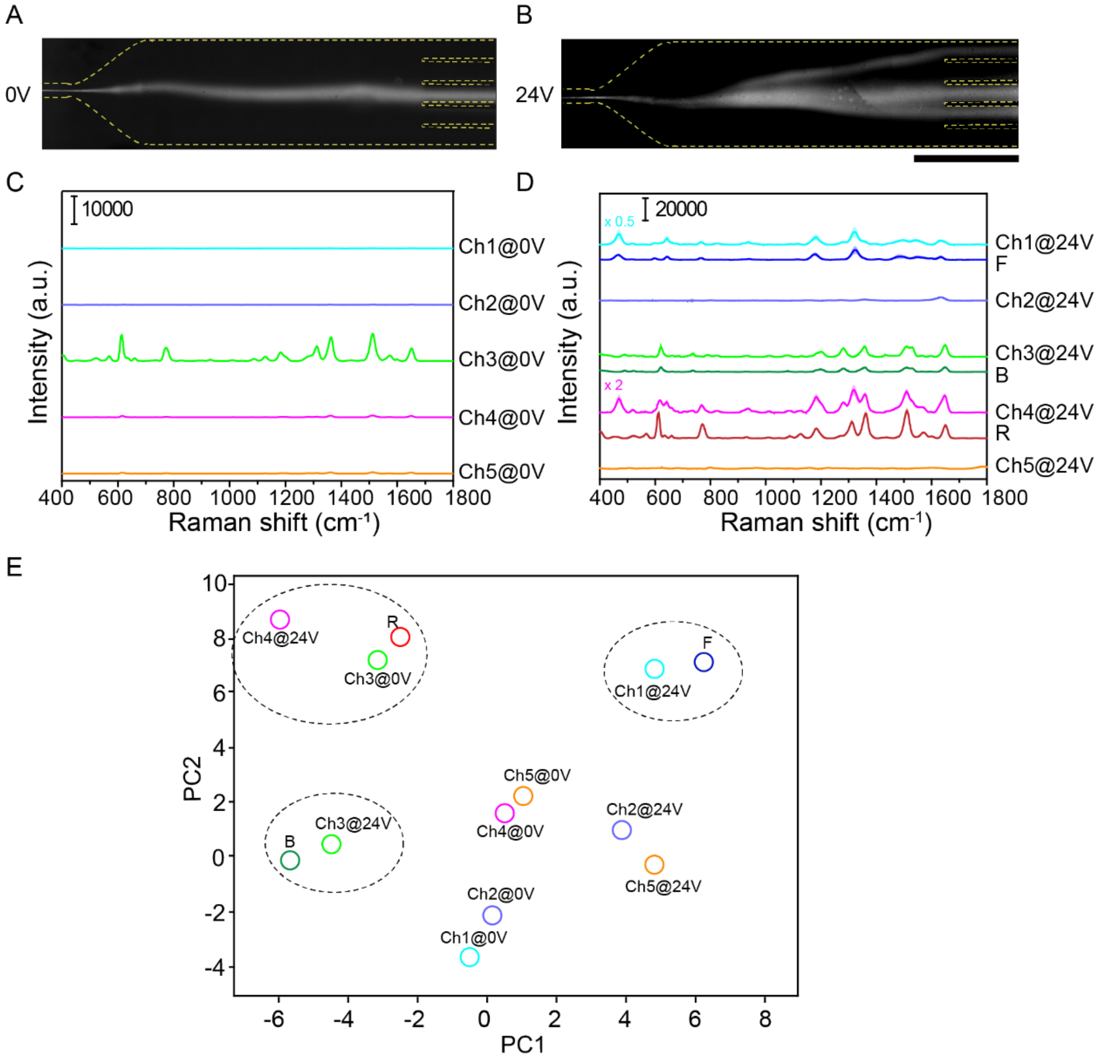

Figure 4-10 The proof-of-concept result for three fluorescent dyes flowed into the FFE-SERS system. The fluorescent image under (A) 0 V. (B) 24 V. The SERS spectrum under

(C) 0 V (D) 24 V. (E) PCA result of the SERS spectrum from five outlets of the FFE channel under 0 V and 24 V.

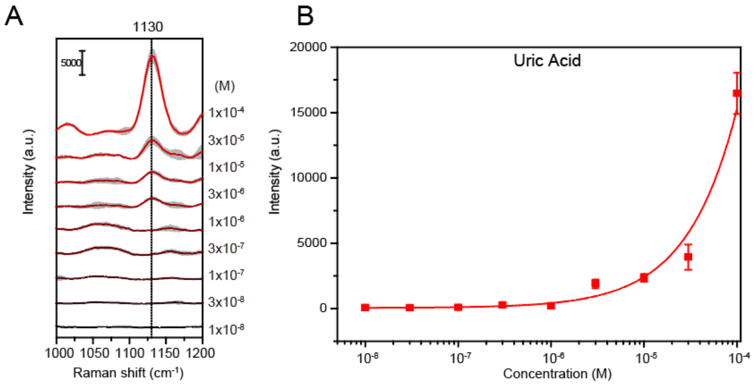

Figure 4-11 The SERS spectrum of purine derivatives. (A) Uric acid. The standard curve of (B) Uric acid. The dashed line represents the peak value for calibration.

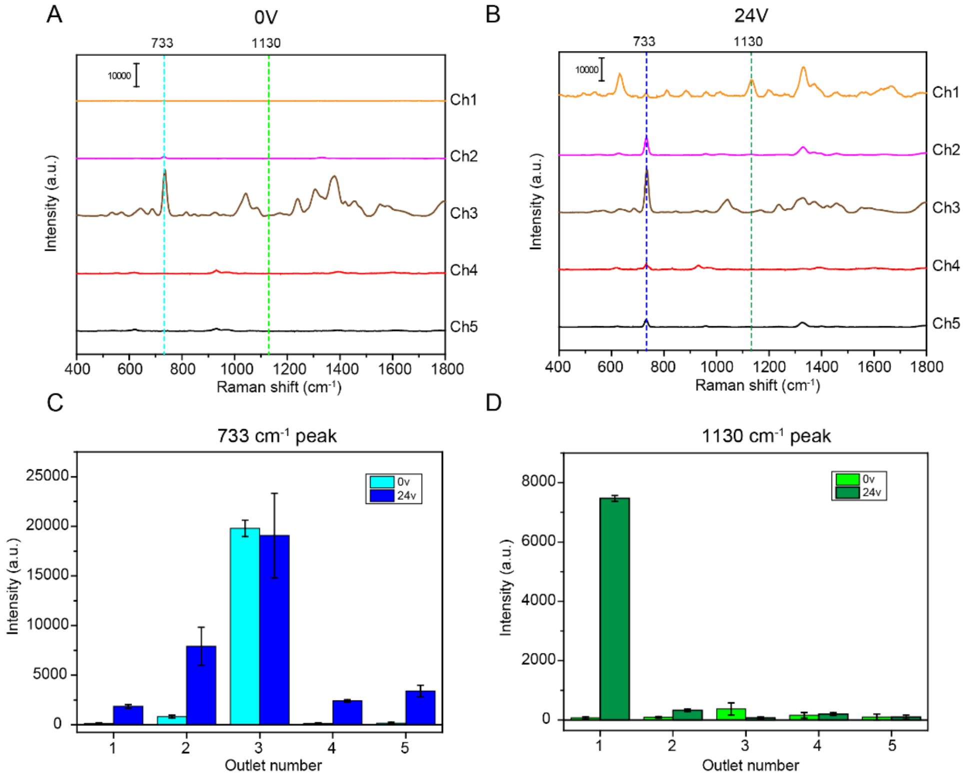

Figure 4-12 The FFE results for purine mixing under (A) 0 V and (B) 24 V; The comparison of peak intensities at Raman shifts of (C) 733 cm^{-1} (D) 1130 cm^{-1} between 0 V and 24 V.

Chapter 5 Conclusions

An integrated μFFE separation and SERS detection microsystem was developed. Initially, we aimed to find the best sheath flow ratio to perform FFE, manipulating the sample properly in a single channel without excessive dilution. Under this ratio, while defining the upper limit of the applied voltage, we determined the optimal buffer and sample flow ratio for the real experiment. Subsequently, FFE experiments were performed on fluorescent samples such as R6G, Rhodamine B, and fluorescein, demonstrating the system's ability to manipulate differently charged samples with various applied voltages, deflecting them into the desired outlets. Furthermore, the quantification capability of the SERS substrate was validated for estimating concentrations in FFE experiments. After calibrating the fluorescent samples with three orders of concentration, we integrated FFE and SERS to conduct online separation and detection of multiplexed samples. Using PCA, we confirmed our ability to separate and detect the mixture of the three fluorescent samples, defining that the concentration would be diluted to 10% after FFE. Finally, we applied a mixture of bacteria metabolites to demonstrate the biological application, considering the pKa of the sample; we adjusted the pH value to pH = 4. The results show that we can separate adenine and uracil, which are the main metabolites of the bacteria.

doi:10.6342/NTU202401456

Chapter 6 Future works

In this thesis, we have demonstrated the integration of FFE separation and SERS detection. However, there is still room for improvement and further applications of this platform.

6.1 Integration of the system on the single chip

Currently, the FFE chip and SERS substrate remain on two separate chips and are connected by the plastic tubing. This arrangement may inadvertently increase the fluid loss and complicate the system. To further simplify the whole system, we aim to modify the device as shown in Figure 6-1. In this process, a thin-film silver is deposited onto a glass slide using the E-beam evaporator, following pre-cleaning of the glass with acetone and sodium hydroxide. A PMMA shadow mask is employed to confine the silver deposition to the size of the SERS separation zone.

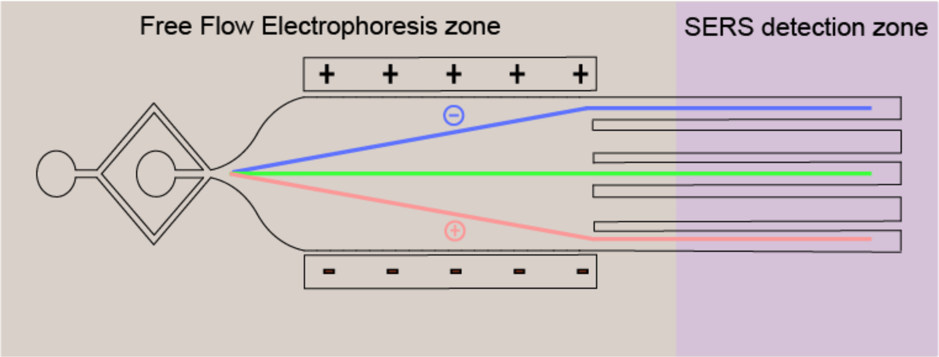

Figure 6-1 The schematic of the integration single chip. The gray square represents the glass slide, while the purple region indicates the deposition of silver nanoparticles.

6.1.1 Preliminary results

We have already tried several methods to integrate the PDMS channel with the SERS substrate. We used the bonding method mentioned in chapter 3.2.1 to avoid damaging the

doi:10.6342/NTU202401456

nano-Ag particles with oxygen plasma. Figure 6-2 shows the result of the bonding process. The bonding was damaged after we applied the voltage for electrophoresis, resulting in fluid leakage. This occurred because the aluminum layer on the substrate was washed out by electrolysis bubbles. To address this issue, we etched the aluminum layer, except for the channel outlet for SERS detection, using 0.1 M NaOH for 10 minutes, as shown in Figure 6-3. However, the substrate was still damaged at the electrode outlet and the main channel outlet. This likely occurred because the PDMS glue used was still susceptible to damage from electrolysis, as its bonding strength was weaker than that of oxygen plasma bonding.

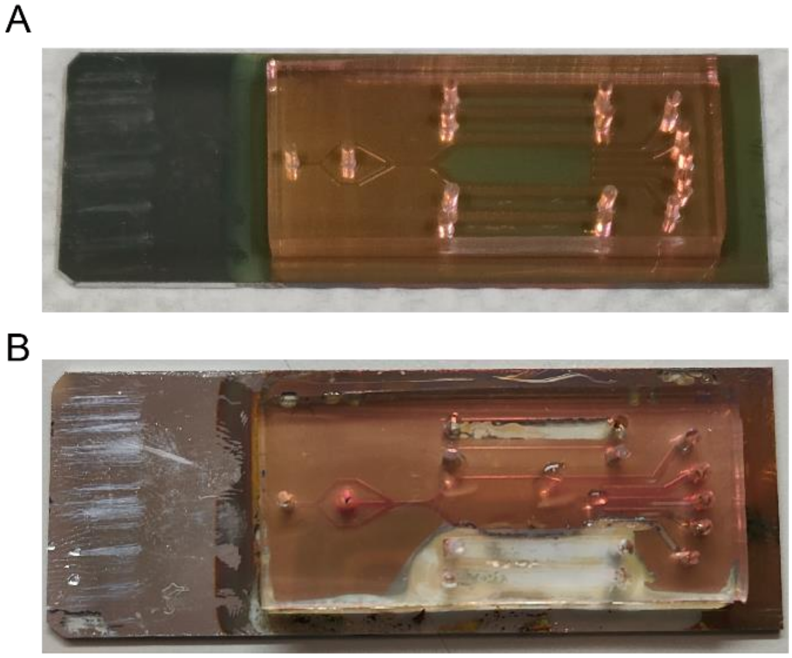

Figure 6-2 Image of the PDMS channel directly bonded to the SERS substrate. (A) Initial state (B) After applying 25 V for 15 minutes.

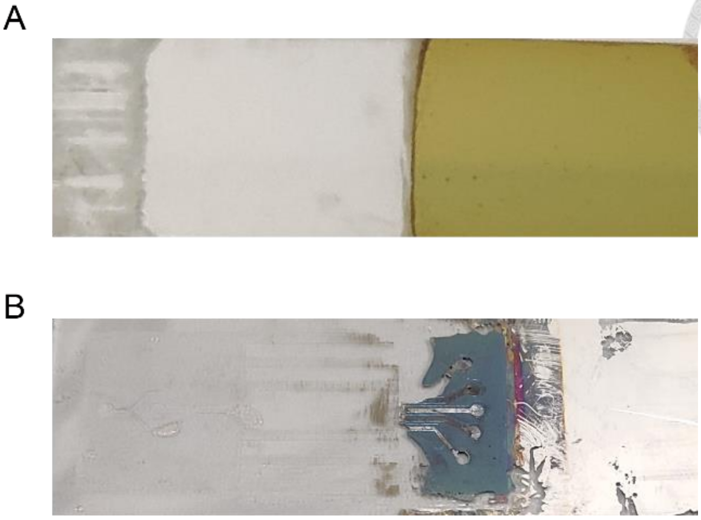

Figure 6-3 Image of the SERS substrate which is an etching by the NaOH (A) Initial state (B) After applying 25 V for 15 minutes.

Based on the above results, direct bonding may be unsuccessful due to electrolysis bubbles potentially damaging the PDMS glue. Here, we can mention two bonding strategies for future work:

(1) Oxygen prevention cover for the channel outlet:

We can design a cover to protect the channel outlet specifically for SERS detection. This would allow us to still perform oxygen plasma bonding while protecting the sensitive areas from electrolysis bubbles.

(2) Guiding channel bonding with the PDMS channel:

We can design a PDMS channel that includes a guiding channel for the separated sample. This method would facilitate easy bonding using oxygen plasma and allow for straightforward attachment to the SERS substrate for detection.

6.2 Cell lysis component analysis

The integrated system offers the advantage of generating multiple signals for the analysis of complex systems. An example is the analysis of cancer cell components through lysis. H. Nam *et al.* employed acoustofluidics to lyse malignant breast cancer cells and measured the SERS spectrum [151]. The results indicated the detection of various organic compounds such as glycogen or proteins that may go undetected without lysis (Figure 6-4). However, the characteristic peak intensity remained low compared to the standard deviation, suggesting potential challenges in detection when the lysis components are mixed. With our platform, we can separate and purify different substances based on their electrophoretic mobility, allowing for higher detection accuracy.

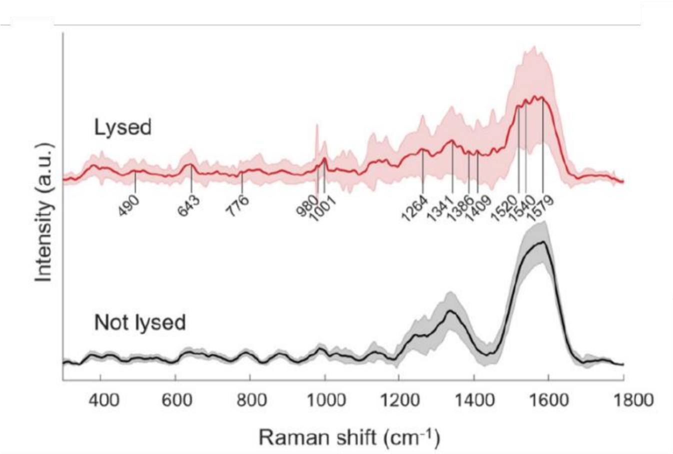

Figure 6-4 SERS spectra for cancer cells with and without lysis. Specific peaks denote presumed organic matter [151].

6.3 Analysis of bacteria due to external stimulation

The mechanism of bacteria under external stimulation, such as light, heat, or ultrasound, has been studied. Different species may exhibit varying responses. For example, W. Liu *et al.* utilized external stress to identify bacteria, applying three stressors—UV, ultrasound, and ethanol—to differentiate four types of bacteria [152]. They asserted that under optimal environmental stress, the SERS spectral differences of bacteria would significantly increase (Figure 6-5). However, they did not analyze the actual biomolecules or metabolites under these stimulations. Additionally, in their experiment, multiple steps were required to purify the bacteria, potentially introducing human error. Our platform not only facilitates sample preprocessing but also enables the investigation of detailed information about metabolites. Moreover, our platform can gather multiple pieces of information for one strain, which is crucial for machine learning applications.

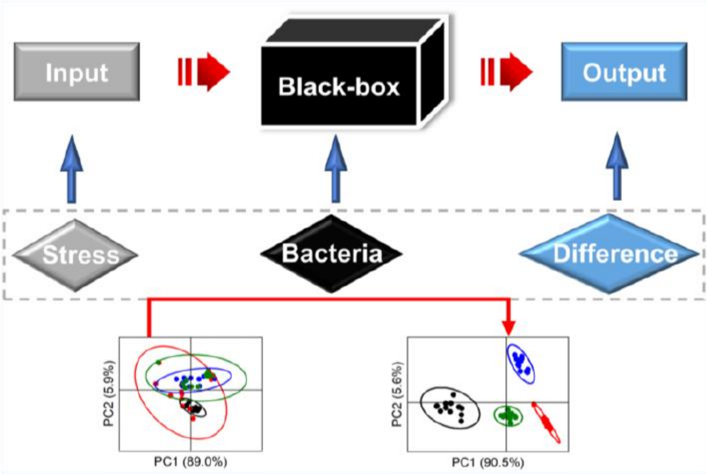

Figure 6-5 Schematic diagram of a black-box approach for bacterial differentiation [152].

References

[1] D. Voytas, "Agarose Gel Electrophoresis," *Current Protocols in Molecular Biology,* vol. 51, no. 1, pp. 2.5A.1-2.5A.9, 2000, doi: https://doi.org/10.1002/0471142727.mb0205as51.

[2] P. Nanthasurasak, J. M. Cabot, H. H. See, R. M. Guijt, and M. C. Breadmore, "Electrophoretic separations on paper: Past, present, and future-A review," *Analytica Chimica Acta,* vol. 985, pp. 7-23, 2017/09/08/ 2017, doi: https://doi.org/10.1016/j.aca.2017.06.015.

[3] B. Sanchez-Vega, "Capillary Electrophoresis of DNA," in *Molecular Biomethods Handbook*, J. M. Walker and R. Rapley Eds. Totowa, NJ: Humana Press, 2008, pp. 65-87.

[4] R. T. Turgeon and M. T. Bowser, "Micro free-flow electrophoresis: theory and applications," *Analytical and Bioanalytical Chemistry,* vol. 394, no. 1, pp. 187-198, 2009/05/01 2009, doi: 10.1007/s00216-009-2656-5.

[5] P. Y. Lee, N. Saraygord-Afshari, and T. Y. Low, "The evolution of two-dimensional gel electrophoresis - from proteomics to emerging alternative applications," *Journal of Chromatography A,* vol. 1615, p. 460763, 2020/03/29/ 2020, doi: https://doi.org/10.1016/j.chroma.2019.460763.

[6] D. Rouquié, A. Capt, W. H. Eby, V. Sekar, and C. Hérouet-Guicheney, "Investigation of endogenous soybean food allergens by using a 2-dimensional gel electrophoresis approach," *Regulatory Toxicology and Pharmacology,* vol. 58, no. 3, Supplement, pp. S47-S53, 2010/12/01/ 2010, doi: https://doi.org/10.1016/j.yrtph.2010.09.013.

[7] C. L. S. Chagas *et al.*, "A fully disposable paper-based electrophoresis microchip with integrated pencil-drawn electrodes for contactless conductivity detection," *Analytical Methods,* 10.1039/C6AY01963C vol. 8, no. 37, pp. 6682-6686, 2016, doi: 10.1039/C6AY01963C.

[8] K. Zamuruyev, M. S. Ferreira Santos, M. F. Mora, E. A. Kurfman, A. C. Noell, and P. A. Willis, "Automated Capillary Electrophoresis System Compatible with Multiple Detectors for Potential In Situ Spaceflight Missions," *Analytical Chemistry,* vol. 93, no. 27, pp. 9647-9655, 2021/07/13 2021, doi: 10.1021/acs.analchem.1c02119.

[9] M. Wang *et al.*, "A platform method for plasmid isoforms analysis by capillary gel electrophoresis," *ELECTROPHORESIS,* vol. 43, no. 11, pp. 1174-1182, 2022, doi: https://doi.org/10.1002/elps.202100343.

[10] W. S. Ramsey, E. D. Nowlan, and L. B. Simpson, "Resolution of microbial mixtures by free flow electrophoresis," *European journal of applied microbiology and biotechnology,* vol. 9, no. 3, pp. 217-226, 1980/09/01 1980, doi: 10.1007/BF00504488.

[11] R. Kuhn and H. Wagner, "Free flow electrophoresis as a method for the purification of enzymes from E. coli cell extract," *ELECTROPHORESIS,* vol. 10, no. 3, pp. 165-172, 1989, doi: https://doi.org/10.1002/elps.1150100302.

[12] S. Staubach *et al.*, "Free flow electrophoresis allows quick and reproducible preparation of extracellular vesicles from conditioned cell culture media," *Extracellular Vesicles and Circulating Nucleic Acids,* vol. 3, no. 1, pp. 31-48, 2022.

[13] A. C. Johnson and M. T. Bowser, "Micro free flow electrophoresis," (in eng), *Lab*

doi:10.6342/NTU202401456

Chip, vol. 18, no. 1, pp. 27-40, Dec 19 2017, doi: 10.1039/c7lc01105a.

[14] D. E. Raymond, A. Manz, and H. M. Widmer, "Continuous Sample Pretreatment Using a Free-Flow Electrophoresis Device Integrated onto a Silicon Chip," *Analytical Chemistry,* vol. 66, no. 18, pp. 2858-2865, 1994/09/15 1994, doi: 10.1021/ac00090a011.

[15] F. J. Agostino and S. N. Krylov, "Advances in steady-state continuous-flow purification by small-scale free-flow electrophoresis," *TrAC Trends in Analytical Chemistry,* vol. 72, pp. 68-79, 2015.

[16] D. Kohlheyer, J. C. Eijkel, A. van den Berg, and R. B. Schasfoort, "Miniaturizing free-flow electrophoresis - a critical review," (in eng), *Electrophoresis,* vol. 29, no. 5, pp. 977-93, Mar 2008, doi: 10.1002/elps.200700725.

[17] Y. Lee and J.-S. Kwon, "Microfluidic free-flow electrophoresis: A promising tool for protein purification and analysis in proteomics," *Journal of Industrial and Engineering Chemistry,* vol. 109, pp. 79-99, 2022/05/25/ 2022, doi: https://doi.org/10.1016/j.jiec.2022.02.028.

[18] P. Novo and D. Janasek, "Current advances and challenges in microfluidic free-flow electrophoresis—A critical review," *Analytica Chimica Acta,* vol. 991, pp. 9-29, 2017/10/23/ 2017, doi: https://doi.org/10.1016/j.aca.2017.08.017.

[19] K. L. Saar, T. Müller, J. r. m. Charmet, P. K. Challa, and T. P. Knowles, "Enhancing the resolution of micro free flow electrophoresis through spatially controlled sample injection," *Analytical chemistry,* vol. 90, no. 15, pp. 8998-9005, 2018. [Online]. Available: https://pubs.acs.org/doi/pdf/10.1021/acs.analchem.8b01205.

[20] X. Fu, N. Mavrogiannis, M. Ibo, F. Crivellari, and Z. R. Gagnon, "Microfluidic free-flow zone electrophoresis and isotachophoresis using carbon black nano-composite PDMS sidewall membranes," *ELECTROPHORESIS,* vol. 38, no. 2, pp. 327-334, 2017, doi: https://doi.org/10.1002/elps.201600104.

[21] S. Köhler, C. Benz, H. Becker, E. Beckert, V. Beushausen, and D. Belder, "Micro free-flow electrophoresis with injection molded chips," *Rsc Advances,* vol. 2, no. 2, pp. 520-525, 2012.

[22] T. Akagi, R. Kubota, M. Kobayashi, and T. Ichiki, "Development of a polymer-based easy-to-fabricate micro-free-flow electrophoresis device," *Japanese Journal of Applied Physics,* vol. 54, no. 6S1, p. 06FN05, 2015.

[23] J. Wen, J. W. Albrecht, and K. F. Jensen, "Microfluidic preparative free-flow isoelectric focusing in a triangular channel: System development and characterization," *ELECTROPHORESIS,* https://doi.org/10.1002/elps.200900577 vol. 31, no. 10, pp. 1606-1614, 2010/05/01 2010, doi: https://doi.org/10.1002/elps.200900577.

[24] J. Wen, E. W. Wilker, M. B. Yaffe, and K. F. Jensen, "Microfluidic Preparative Free-Flow Isoelectric Focusing: System Optimization for Protein Complex Separation," *Analytical Chemistry,* vol. 82, no. 4, pp. 1253-1260, 2010/02/15 2010, doi: 10.1021/ac902157e.

[25] F. J. Agostino, L. T. Cherney, V. Galievsky, and S. N. Krylov, "Steady-state continuous-flow purification by electrophoresis," *Angewandte Chemie International Edition,* vol. 52, no. 28, pp. 7256-7260, 2013. [Online]. Available: https://onlinelibrary.wiley.com/doi/pdfdirect/10.1002/anie.201300104?download=true.

[26] T. Herling, T. Müller, L. Rajah, J. Skepper, M. Vendruscolo, and T. Knowles, "Integration and characterization of solid wall electrodes in microfluidic devices fabricated in a single photolithography step," *Applied physics letters,* vol. 102, no.

doi:10.6342/NTU202401456

18, p. 184102, 2013.

[27] J. A. Preuss, G. N. Nguyen, V. Berk, and J. Bahnemann, "Miniaturized free-flow electrophoresis: production, optimization, and application using 3D printing technology," *Electrophoresis,* vol. 42, no. 3, pp. 305-314, 2021. [Online]. Available: https://analyticalsciencejournals.onlinelibrary.wiley.com/doi/pdfdirect/10.1002/elps.202000149?download=true.

[28] S. Köhler, C. Weilbeer, S. Howitz, H. Becker, V. Beushausen, and D. Belder, "PDMS free-flow electrophoresis chips with integrated partitioning bars for bubble segregation," *Lab on a Chip,* vol. 11, no. 2, pp. 309-314, 2011. [Online]. Available: https://pubs.rsc.org/en/content/articlepdf/2011/lc/c0lc00347f.

[29] P. Novo, M. Dell'Aica, M. Jender, S. Höving, R. P. Zahedi, and D. Janasek, "Integration of polycarbonate membranes in microfluidic free-flow electrophoresis," *Analyst,* vol. 142, no. 22, pp. 4228-4239, 2017. [Online]. Available: https://pubs.rsc.org/en/content/articlepdf/2017/an/c7an01514c.

[30] P. Novo, M. Jender, M. Dell'Aica, R. P. Zahedi, and D. Janasek, "Free flow electrophoresis separation of proteins and DNA using microfluidics and polycarbonate membranes," *Procedia Engineering,* vol. 168, pp. 1382-1385, 2016.

[31] E. Poehler *et al.*, "Label-free microfluidic free-flow isoelectric focusing, pH gradient sensing and near real-time isoelectric point determination of biomolecules and blood plasma fractions," *Analyst,* 10.1039/C5AN01345C vol. 140, no. 22, pp. 7496-7502, 2015, doi: 10.1039/C5AN01345C.

[32] H. Ding *et al.*, "Fabrication of micro free-flow electrophoresis chip by photocurable monomer binding microfabrication technique for continuous separation of proteins and their numerical simulation," *Analyst,* vol. 137, no. 19, pp. 4482-4489, 2012. [Online]. Available: https://pubs.rsc.org/en/content/articlepdf/2012/an/c2an35535c.

[33] G. Krainer *et al.*, "Direct digital sensing of protein biomarkers in solution," *Nature Communications,* vol. 14, no. 1, p. 653, 2023/02/06 2023, doi: 10.1038/s41467-023-35792-x.

[34] M. Becker, C. Budich, V. Deckert, and D. Janasek, "Isotachophoretic free-flow electrophoretic focusing and SERS detection of myoglobin inside a miniaturized device," *Analyst,* 10.1039/B816717F vol. 134, no. 1, pp. 38-40, 2009, doi: 10.1039/B816717F.

[35] S. Podszun *et al.*, "Enrichment of viable bacteria in a micro-volume by free-flow electrophoresis," *Lab on a Chip,* vol. 12, no. 3, pp. 451-457, 2012. [Online]. Available: https://pubs.rsc.org/en/content/articlepdf/2012/lc/c1lc20575g.

[36] J. E. Prest *et al.*, "Miniaturised free flow isotachophoresis of bacteria using an injection moulded separation device," *Journal of Chromatography B,* vol. 903, pp. 53-59, 2012/08/15/ 2012, doi: https://doi.org/10.1016/j.jchromb.2012.06.040.

[37] F. Barbaresco, M. Cocuzza, C. F. Pirri, and S. L. Marasso, "Application of a Micro Free-Flow Electrophoresis 3D Printed Lab-on-a-Chip for Micro-Nanoparticles Analysis," (in eng), *Nanomaterials (Basel),* vol. 10, no. 7, Jun 30 2020, doi: 10.3390/nano10071277.

[38] P. Hoffmann, H. Wagner, G. Weber, M. Lanz, J. Caslavska, and W. Thormann, "Separation and Purification of Methadone Enantiomers by Continuous- and Interval-Flow Electrophoresis," *Analytical Chemistry,* vol. 71, no. 9, pp. 1840-1850, 1999/05/01 1999, doi: 10.1021/ac981178v.

[39] G. Kaigala, M. Bercovici, M. Behnam, D. Elliott, J. Santiago, and C. Backhouse,

doi:10.6342/NTU202401456

"Miniaturized system for isotachophoresis assays," *Lab on a Chip,* vol. 10, no. 17, pp. 2242-2250, 2010. [Online]. Available: https://pubs.rsc.org/en/content/articlepdf/2010/lc/c004120c.

[40] T. Haensch *et al.*, "Integration of Impedimetric Sensors for In Situ Electrochemical Impedance Spectroscopy in Free-Flow Electrophoresis Applications in Lab-on-Chip Systems," *ACS sensors,* 2022.

[41] M. Hügle, O. Behrmann, M. Raum, F. T. Hufert, G. A. Urban, and G. Dame, "A lab-on-a-chip for free-flow electrophoretic preconcentration of viruses and gel electrophoretic DNA extraction," *Analyst,* vol. 145, no. 7, pp. 2554-2561, 2020.

[42] M. Jender, P. Novo, D. Maehler, U. Münchberg, D. Janasek, and E. Freier, "Multiplexed online monitoring of microfluidic free-flow electrophoresis via mass spectrometry," *Analytical chemistry,* vol. 92, no. 9, pp. 6764-6769, 2020. [Online]. Available: https://pubs.acs.org/doi/pdf/10.1021/acs.analchem.0c00996.

[43] R. Panneerselvam, H. Sadat, E. M. Höhn, A. Das, H. Noothalapati, and D. Belder, "Microfluidics and surface-enhanced Raman spectroscopy, a win-win combination?," (in eng), *Lab Chip,* vol. 22, no. 4, pp. 665-682, Feb 15 2022, doi: 10.1039/d1lc01097b.

[44] S. Bai, X. Ren, K. Obata, Y. Ito, and K. Sugioka, "Label-free trace detection of bio-molecules by liquid-interface assisted surface-enhanced Raman scattering using a microfluidic chip," *Opto-Electronic Advances,* vol. 5, no. 10, pp. 210121-1-210121-10, 2022/08/20 2022, doi: 10.29026/oea.2022.210121.

[45] H. Pu, W. Xiao, and D.-W. Sun, "SERS-microfluidic systems: A potential platform for rapid analysis of food contaminants," *Trends in Food Science & Technology,* vol. 70, pp. 114-126, 2017/12/01/ 2017, doi: https://doi.org/10.1016/j.tifs.2017.10.001.

[46] J. Guo, F. Zeng, J. Guo, and X. Ma, "Preparation and application of microfluidic SERS substrate: Challenges and future perspectives," *Journal of Materials Science & Technology,* vol. 37, pp. 96-103, 2020.

[47] H. Lu, L. Zhu, C. Zhang, K. Chen, and Y. Cui, "Mixing Assisted “Hot Spots” Occupying SERS Strategy for Highly Sensitive In Situ Study," *Analytical Chemistry,* vol. 90, no. 7, pp. 4535-4543, 2018/04/03 2018, doi: 10.1021/acs.analchem.7b04929.

[48] G. Chen *et al.*, "A highly sensitive microfluidics system for multiplexed surface-enhanced Raman scattering (SERS) detection based on Ag nanodot arrays," *RSC Advances,* 10.1039/C4RA09251A vol. 4, no. 97, pp. 54434-54440, 2014, doi: 10.1039/C4RA09251A.

[49] N. Choi *et al.*, "Integrated SERS-based microdroplet platform for the automated immunoassay of F1 antigens in Yersinia pestis," *Analytical chemistry,* vol. 89, no. 16, pp. 8413-8420, 2017.

[50] S. Dey *et al.*, "A microfluidic-SERSplatform for isolation and immuno-phenotyping of antigen specific T-cells," *Sensors and Actuators B: Chemical,* vol. 284, pp. 281-288, 2019.

[51] R. Gao *et al.*, "Fast and sensitive detection of an anthrax biomarker using SERS-based solenoid microfluidic sensor," *Biosensors and Bioelectronics,* vol. 72, pp. 230-236, 2015.

[52] R. Gao *et al.*, "SERS-based pump-free microfluidic chip for highly sensitive immunoassay of prostate-specific antigen biomarkers," *ACS sensors,* vol. 4, no. 4, pp. 938-943, 2019.

[53] A. Kamińska, E. Witkowska, K. Winkler, I. Dzięcielewski, J. L. Weyher, and J.

Waluk, "Detection of Hepatitis B virus antigen from human blood: SERS immunoassay in a microfluidic system," *Biosensors and bioelectronics,* vol. 66, pp. 461-467, 2015.
[54] M. Lee, K. Lee, K. H. Kim, K. W. Oh, and J. Choo, "SERS-based immunoassay using a gold array-embedded gradient microfluidic chip," *Lab on a Chip,* vol. 12, no. 19, pp. 3720-3727, 2012.
[55] Z. Zheng, L. Wu, L. Li, S. Zong, Z. Wang, and Y. Cui, "Simultaneous and highly sensitive detection of multiple breast cancer biomarkers in real samples using a SERS microfluidic chip," *Talanta,* vol. 188, pp. 507-515, 2018.
[56] X. Cao *et al.*, "A pump-free and high-throughput microfluidic chip for highly sensitive SERS assay of gastric cancer-related circulating tumor DNA via a cascade signal amplification strategy," *Journal of Nanobiotechnology,* vol. 20, no. 1, pp. 1-13, 2022.
[57] X. Cao *et al.*, "A dual-signal amplification strategy based on pump-free SERS microfluidic chip for rapid and ultrasensitive detection of non-small cell lung cancer-related circulating tumour DNA in mice serum," *Biosensors and Bioelectronics,* vol. 205, p. 114110, 2022.
[58] N. Choi *et al.*, "Simultaneous detection of duplex DNA oligonucleotides using a SERS-based micro-network gradient chip," *Lab on a Chip,* vol. 12, no. 24, pp. 5160-5167, 2012.
[59] L. Ma, S. Ye, X. Wang, and J. Zhang, "SERS-microfluidic approach for the quantitative detection of miRNA using DNAzyme-mediated reciprocal signal amplification," *ACS sensors,* vol. 6, no. 3, pp. 1392-1399, 2021.
[60] T. Park *et al.*, "Highly sensitive signal detection of duplex dye-labelled DNA oligonucleotides in a PDMS microfluidic chip: confocal surface-enhanced Raman spectroscopic study," *Lab on a Chip,* vol. 5, no. 4, pp. 437-442, 2005.
[61] K. K. Strelau, R. Kretschmer, R. Möller, W. Fritzsche, and J. Popp, "SERS as tool for the analysis of DNA-chips in a microfluidic platform," *Analytical and bioanalytical chemistry,* vol. 396, pp. 1381-1384, 2010.
[62] L. Wu *et al.*, "Amplification-free SERS analysis of DNA mutation in cancer cells with single-base sensitivity," *Nanoscale,* vol. 11, no. 16, pp. 7781-7789, 2019.
[63] I. Freitag, C. Beleites, S. Dochow, J. Clement, C. Krafft, and J. Popp, "Recognition of tumor cells by immuno-SERS-markers in a microfluidic chip at continuous flow," *Analyst,* vol. 141, no. 21, pp. 5986-5989, 2016.
[64] Z. Qian *et al.*, "In situ visualization and SERS monitoring of the interaction between tumor and endothelial cells using 3D microfluidic networks," *ACS sensors,* vol. 5, no. 1, pp. 208-216, 2019.
[65] Y. Zhang, Z. Wang, L. Wu, S. Zong, B. Yun, and Y. Cui, "Combining multiplex SERS nanovectors and multivariate analysis for in situ profiling of circulating tumor cell phenotype using a microfluidic chip," *Small,* vol. 14, no. 20, p. 1704433, 2018.
[66] Y. Zhang, L. Wu, K. Yang, S. Zong, Z. Wang, and Y. Cui, "2D profiling of tumor chemotactic and molecular phenotype at single cell resolution using a SERS-microfluidic chip," *Nano Research,* vol. 15, no. 5, pp. 4357-4365, 2022.
[67] H. T. Ngo, H.-N. Wang, A. M. Fales, and T. Vo-Dinh, "Plasmonic SERS biosensing nanochips for DNA detection," *Analytical and Bioanalytical Chemistry,* vol. 408, no. 7, pp. 1773-1781, 2016/03/01 2016, doi: 10.1007/s00216-015-9121-4.
[68] Z. Wang *et al.*, "Screening and multiple detection of cancer exosomes using an

doi:10.6342/NTU202401456

SERS-based method," *Nanoscale,* 10.1039/C7NR09162A vol. 10, no. 19, pp. 9053-9062, 2018, doi: 10.1039/C7NR09162A.

[69] T. T. Ong, E. W. Blanch, and O. A. Jones, "Surface Enhanced Raman Spectroscopy in environmental analysis, monitoring and assessment," *Science of The Total Environment,* vol. 720, p. 137601, 2020.

[70] S. Bai, D. Serien, A. Hu, and K. Sugioka, "3D microfluidic Surface-Enhanced Raman Spectroscopy (SERS) chips fabricated by all-femtosecond-laser-processing for real-time sensing of toxic substances," *Advanced Functional Materials,* vol. 28, no. 23, p. 1706262, 2018.

[71] W. Cui, Z. Ren, Y. Song, and C. L. Ren, "Development and potential for point-of-care heavy metal sensing using microfluidic systems: A brief review," *Sensors and Actuators A: Physical,* p. 113733, 2022.

[72] M.-K. Filippidou and S. Chatzandroulis, "Microfluidic Devices for Heavy Metal Ions Detection: A Review," *Micromachines,* vol. 14, no. 8, p. 1520, 2023.

[73] X. He, X. Zhou, Y. Liu, and X. Wang, "Ultrasensitive, recyclable and portable microfluidic surface-enhanced raman scattering (SERS) biosensor for uranyl ions detection," *Sensors and Actuators B: Chemical,* vol. 311, p. 127676, 2020.

[74] J. P. Lafleur, S. Senkbeil, T. G. Jensen, and J. P. Kutter, "Gold nanoparticle-based optical microfluidic sensors for analysis of environmental pollutants," *Lab on a Chip,* vol. 12, no. 22, pp. 4651-4656, 2012.

[75] Y. Lin, D. Gritsenko, S. Feng, Y. C. Teh, X. Lu, and J. Xu, "Detection of heavy metal by paper-based microfluidics," *Biosensors and Bioelectronics,* vol. 83, pp. 256-266, 2016.

[76] D. Liu, C. Liu, Y. Yuan, X. Zhang, Y. Huang, and S. Yan, "Microfluidic Transport of Hybrid Optoplasmonic Particles for Repeatable SERS Detection," *Analytical Chemistry,* vol. 93, no. 30, pp. 10672-10678, 2021.

[77] S. Yan *et al.*, "Rapid, one-step preparation of SERS substrate in microfluidic channel for detection of molecules and heavy metal ions," *Spectrochimica Acta Part A: Molecular and Biomolecular Spectroscopy,* vol. 220, p. 117113, 2019/09/05/ 2019, doi: https://doi.org/10.1016/j.saa.2019.05.018.

[78] H. Zhang, D. Wang, D. Zhang, T. Zhang, L. Yang, and Z. Li, "In Situ Microfluidic SERS Chip for Ultrasensitive Hg2+ Sensing Based on I—Functionalized Silver Aggregates," *ACS Applied Materials & Interfaces,* vol. 14, no. 1, pp. 2211-2218, 2021.

[79] M. T. Alula, Z. T. Mengesha, and E. Mwenesongole, "Advances in surface-enhanced Raman spectroscopy for analysis of pharmaceuticals: A review," *Vibrational Spectroscopy,* vol. 98, pp. 50-63, 2018.

[80] V. Burtsev *et al.*, "Detection of trace amounts of insoluble pharmaceuticals in water by extraction and SERS measurements in a microfluidic flow regime," *Analyst,* vol. 146, no. 11, pp. 3686-3696, 2021.

[81] D. Craig, M. Mazilu, and K. Dholakia, "Quantitative detection of pharmaceuticals using a combination of paper microfluidics and wavelength modulated Raman spectroscopy," *PLoS One,* vol. 10, no. 5, p. e0123334, 2015.

[82] P. Cui and S. Wang, "Application of microfluidic chip technology in pharmaceutical analysis: A review," *Journal of pharmaceutical analysis,* vol. 9, no. 4, pp. 238-247, 2019.

[83] Y. Gutiérrez *et al.*, "Paving the Way to Industrially Fabricated Disposable and Customizable Surface-Enhanced Raman Scattering Microfluidic Chips for Diagnostic Applications," *Advanced Engineering Materials,* vol. 24, no. 8, p.

2101365, 2022.

[84] Y. H. Kim, D. J. Kim, S. Lee, D. H. Kim, S. G. Park, and S. H. Kim, "Microfluidic designing microgels containing highly concentrated gold nanoparticles for SERS analysis of complex fluids," *Small,* vol. 15, no. 52, p. 1905076, 2019.

[85] N. D. Kline *et al.*, "Optimization of surface-enhanced Raman spectroscopy conditions for implementation into a microfluidic device for drug detection," *Analytical chemistry,* vol. 88, no. 21, pp. 10513-10522, 2016.

[86] S. Li *et al.*, "Dynamic SPME–SERS induced by electric field: toward in situ monitoring of pharmaceuticals and personal care products," *Analytical Chemistry,* vol. 94, no. 26, pp. 9270-9277, 2022.

[87] A. März *et al.*, "The multifunctional application of microfluidic lab-on-a-chip surface enhanced Raman spectroscopy (LOC-SERS) within the field of bioanalytics," in *European Conference on Biomedical Optics*, 2011: Optica Publishing Group, p. 808707.

[88] S. Patze, U. Huebner, F. Liebold, K. Weber, D. Cialla-May, and J. Popp, "SERS as an analytical tool in environmental science: the detection of sulfamethoxazole in the nanomolar range by applying a microfluidic cartridge setup," *Analytica chimica acta,* vol. 949, pp. 1-7, 2017.

[89] Z. Jiang, Y. Zhuang, S. Guo, A. M. F. Sohan, and B. Yin, "Advances in Microfluidics Techniques for Rapid Detection of Pesticide Residues in Food," *Foods,* vol. 12, no. 15, p. 2868, 2023.

[90] Y. Li, S. Yang, C. Qu, Z. Ding, and H. Liu, "Hydrogel-based surface-enhanced Raman spectroscopy for food contaminant detection: A review on classification, strategies, and applications," *Food Safety and Health,* 2023.

[91] P. Murugesan, G. Raj, and J. Moses, "Microfluidic devices for the detection of pesticide residues," *Reviews in Environmental Science and Bio/Technology,* vol. 22, no. 3, pp. 625-652, 2023.

[92] R. Ray *et al.*, "based microfluidic devices for food adulterants: Cost-effective technological monitoring systems," *Food Chemistry,* vol. 390, p. 133173, 2022.

[93] A. Tsagkaris, J. Pulkrabova, and J. Hajslova, "Optical Screening Methods for Pesticide Residue Detection in Food Matrices: Advances and Emerging Analytical Trends. Foods 2021, 10, 88," *Novel Analytical Methods in Food Analysis,* p. 125, 2021.

[94] Y. Wang *et al.*, "A 3D spongy flexible nanosheet array for on-site recyclable swabbing extraction and subsequent SERS analysis of thiram," *Microchimica Acta,* vol. 186, pp. 1-9, 2019.

[95] J. Xie, H. Pang, R. Sun, T. Wang, X. Meng, and Z. Zhou, "Development of rapid and high-precision colorimetric device for organophosphorus pesticide detection based on microfluidic mixer chip," *Micromachines,* vol. 12, no. 3, p. 290, 2021.

[96] G. Emonds-Alt *et al.*, "Development and validation of an integrated microfluidic device with an in-line Surface Enhanced Raman Spectroscopy (SERS) detection of glyphosate in drinking water," *Talanta,* vol. 249, p. 123640, 2022/11/01/ 2022, doi: https://doi.org/10.1016/j.talanta.2022.123640.

[97] D. Zhang, H. Pu, L. Huang, and D.-W. Sun, "Advances in flexible surface-enhanced Raman scattering (SERS) substrates for nondestructive food detection: Fundamentals and recent applications," *Trends in Food Science & Technology,* vol. 109, pp. 690-701, 2021/03/01/ 2021, doi: https://doi.org/10.1016/j.tifs.2021.01.058.

[98] O.-M. Buja, O. D. Gordan, N. Leopold, A. Morschhauser, J. Nestler, and D. R.

Zahn, "Microfluidic setup for on-line SERS monitoring using laser induced nanoparticle spots as SERS active substrate," *Beilstein Journal of Nanotechnology,* vol. 8, no. 1, pp. 237-243, 2017.

[99] S. Lee *et al.*, "Fast and sensitive trace analysis of malachite green using a surface-enhanced Raman microfluidic sensor," *Analytica chimica acta,* vol. 590, no. 2, pp. 139-144, 2007.

[100] B. Liu *et al.*, "A Surface Enhanced Raman Scattering (SERS) microdroplet detector for trace levels of crystal violet," *Microchimica Acta,* vol. 180, pp. 997-1004, 2013.

[101] B. Liu, T. Wu, X. Yang, Z. Wang, and Y. Du, "Portable microfluidic chip based surface-enhanced raman spectroscopy sensor for crystal violet," *Analytical Letters,* vol. 47, no. 16, pp. 2682-2690, 2014.

[102] J. Parisi, Q. Dong, and Y. Lei, "In situ microfluidic fabrication of SERS nanostructures for highly sensitive fingerprint microfluidic-SERS sensing," *RSC advances,* vol. 5, no. 19, pp. 14081-14089, 2015.

[103] R. Wang *et al.*, "A microfluidic chip based on an ITO support modified with Ag-Au nanocomposites for SERS based determination of melamine," *Microchimica Acta,* vol. 184, no. 1, pp. 279-287, 2017/01/01 2017, doi: 10.1007/s00604-016-1990-5.

[104] S. H. Yazdi and I. M. White, "Multiplexed detection of aquaculture fungicides using a pump-free optofluidic SERS microsystem," *Analyst,* 10.1039/C2AN36232E vol. 138, no. 1, pp. 100-103, 2013, doi: 10.1039/C2AN36232E.

[105] H. Alawadhi *et al.*, "Trace-level sensing of food toxins by flexible and cost-effective SERS sensors fabricated by pulsed-laser-deposition of gold nanoparticles on polycarbonate matrix," *Surfaces and Interfaces,* p. 103016, 2023.

[106] S. Bai, D. Serien, Y. Ma, K. Obata, and K. Sugioka, "Attomolar sensing based on liquid interface-assisted surface-enhanced Raman scattering in microfluidic chip by femtosecond laser processing," *ACS Applied Materials & Interfaces,* vol. 12, no. 37, pp. 42328-42338, 2020.

[107] A. Bernat, M. Samiwala, J. Albo, X. Jiang, and Q. Rao, "Challenges in SERS-based pesticide detection and plausible solutions," *Journal of agricultural and food chemistry,* vol. 67, no. 45, pp. 12341-12347, 2019.

[108] Y. Deng, Q. Li, Y. Zhou, and J. Qian, "Fully inkjet printing preparation of a carbon dots multichannel microfluidic paper-based sensor and its application in food additive detection," *ACS Applied Materials & Interfaces,* vol. 13, no. 48, pp. 57084-57091, 2021.

[109] H. Dies, M. Siampani, C. Escobedo, and A. Docoslis, "Direct detection of toxic contaminants in minimally processed food products using dendritic surface-enhanced Raman scattering substrates," *Sensors,* vol. 18, no. 8, p. 2726, 2018.

[110] X. Kong, K. Squire, X. Chong, and A. X. Wang, "Ultra-sensitive lab-on-a-chip detection of Sudan I in food using plasmonics-enhanced diatomaceous thin film," *Food control,* vol. 79, pp. 258-265, 2017.

[111] S. Kumar, A. Deep, N. Wangoo, and N. Bhardwaj, "Recent advancements in nanomaterials based optical detection of food additives: A review," *Analyst,* 2023.

[112] Ü. Dogan *et al.*, "Escherichia coli enumeration in a capillary-driven microfluidic chip with SERS," *Biosensors,* vol. 12, no. 9, p. 765, 2022.

[113] B. Krafft, A. Tycova, R. D. Urban, C. Dusny, and D. Belder, "Microfluidic device for concentration and SERS-based detection of bacteria in drinking water,"

Electrophoresis, vol. 42, no. 1-2, pp. 86-94, 2021.

[114] X. Lu *et al.*, "Detecting and tracking nosocomial methicillin-resistant Staphylococcus aureus using a microfluidic SERS biosensor," *Analytical chemistry,* vol. 85, no. 4, pp. 2320-2327, 2013.

[115] N. A. Mungroo, G. Oliveira, and S. Neethirajan, "SERS based point-of-care detection of food-borne pathogens," *Microchimica acta,* vol. 183, pp. 697-707, 2016.

[116] B. Nasseri, N. Soleimani, N. Rabiee, A. Kalbasi, M. Karimi, and M. R. Hamblin, "Point-of-care microfluidic devices for pathogen detection," *Biosensors and Bioelectronics,* vol. 117, pp. 112-128, 2018.

[117] L. Rodríguez-Lorenzo *et al.*, "Gold nanostars for the detection of foodborne pathogens via surface-enhanced Raman scattering combined with microfluidics," *ACS Applied Nano Materials,* vol. 2, no. 10, pp. 6081-6086, 2019.

[118] C. Wang, F. Madiyar, C. Yu, and J. Li, "Detection of extremely low concentration waterborne pathogen using a multiplexing self-referencing SERS microfluidic biosensor," *Journal of Biological Engineering,* vol. 11, no. 1, pp. 1-11, 2017.

[119] Y. Wang *et al.*, "Duplex microfluidic SERS detection of pathogen antigens with nanoyeast single-chain variable fragments," *Analytical chemistry,* vol. 86, no. 19, pp. 9930-9938, 2014.

[120] M. Viehrig *et al.*, "Quantitative SERS Assay on a Single Chip Enabled by Electrochemically Assisted Regeneration: A Method for Detection of Melamine in Milk," *Analytical Chemistry,* vol. 92, no. 6, pp. 4317-4325, 2020/03/17 2020, doi: 10.1021/acs.analchem.9b05060.

[121] Y. Zhang, S. Zhao, J. Zheng, and L. He, "Surface-enhanced Raman spectroscopy (SERS) combined techniques for high-performance detection and characterization," *TrAC Trends in Analytical Chemistry,* vol. 90, pp. 1-13, 2017/05/01/ 2017, doi: https://doi.org/10.1016/j.trac.2017.02.006.

[122] M. Xie *et al.*, "Key steps for improving bacterial SERS signals in complex samples: Separation, recognition, detection, and analysis," *Talanta,* vol. 268, p. 125281, 2024/02/01/ 2024, doi: https://doi.org/10.1016/j.talanta.2023.125281.

[123] P. Reokrungruang, I. Chatnuntawech, T. Dharakul, and S. Bamrungsap, "A simple paper-based surface enhanced Raman scattering (SERS) platform and magnetic separation for cancer screening," *Sensors and Actuators B: Chemical,* vol. 285, pp. 462-469, 2019/04/15/ 2019, doi: https://doi.org/10.1016/j.snb.2019.01.090.

[124] Y. Wang, S. Ravindranath, and J. Irudayaraj, "Separation and detection of multiple pathogens in a food matrix by magnetic SERS nanoprobes," *Analytical and Bioanalytical Chemistry,* vol. 399, no. 3, pp. 1271-1278, 2011/01/01 2011, doi: 10.1007/s00216-010-4453-6.

[125] K. Rule Wigginton and P. J. Vikesland, "Gold-coated polycarbonate membrane filter for pathogen concentration and SERS-based detection," *Analyst,* 10.1039/B919270K vol. 135, no. 6, pp. 1320-1326, 2010, doi: 10.1039/B919270K.

[126] I.-H. Cho, P. Bhandari, P. Patel, and J. Irudayaraj, "Membrane filter-assisted surface enhanced Raman spectroscopy for the rapid detection of E. coli O157:H7 in ground beef," *Biosensors and Bioelectronics,* vol. 64, pp. 171-176, 2015/02/15/ 2015, doi: https://doi.org/10.1016/j.bios.2014.08.063.

[127] O. Coskun, "Separation techniques: chromatography," *Northern clinics of*

Istanbul, vol. 3, no. 2, p. 156, 2016. [Online]. Available: https://www.ncbi.nlm.nih.gov/pmc/articles/PMC5206469/pdf/NCI-3-156.pdf.

[128] W. Wang, M. Xu, Q. Guo, Y. Yuan, R. Gu, and J. Yao, "Rapid separation and on-line detection by coupling high performance liquid chromatography with surface-enhanced Raman spectroscopy," *RSC Advances,* 10.1039/C5RA05562H vol. 5, no. 59, pp. 47640-47646, 2015, doi: 10.1039/C5RA05562H.

[129] Y.-Y. Wang *et al.*, "A particle-based microfluidic molecular separation integrating surface-enhanced Raman scattering sensing for purine derivatives analysis," *Microfluidics and Nanofluidics,* vol. 23, no. 4, p. 48, 2019/03/04 2019, doi: 10.1007/s10404-019-2216-z.

[130] A. Tycova, R. F. Gerhardt, and D. Belder, "Surface enhanced Raman spectroscopy in microchip electrophoresis," *Journal of Chromatography A,* vol. 1541, pp. 39-46, 2018/03/16/ 2018, doi: https://doi.org/10.1016/j.chroma.2018.02.014.

[131] R. Panneerselvam, H. Sadat, E.-M. Höhn, A. Das, H. Noothalapati, and D. Belder, "Microfluidics and surface-enhanced Raman spectroscopy, a win–win combination?," *Lab on a Chip,* vol. 22, no. 4, pp. 665-682, 2022. [Online]. Available: https://pubs.rsc.org/en/content/articlepdf/2022/lc/d1lc01097b.

[132] D. Cialla-May, M. Schmitt, and J. Popp, "Theoretical principles of Raman spectroscopy," *Physical Sciences Reviews,* vol. 4, 2019.

[133] P. G. Etchegoin and E. C. Le Ru, "Quantifying SERS enhancements," *MRS Bulletin,* vol. 38, no. 8, pp. 631-640, 2013, doi: 10.1557/mrs.2013.158.

[134] A. Campion and P. Kambhampati, "Surface-enhanced Raman scattering," *Chemical Society Reviews,* 10.1039/A827241Z vol. 27, no. 4, pp. 241-250, 1998, doi: 10.1039/A827241Z.

[135] H. Wang *et al.*, "Coupling enhancement mechanisms, materials, and strategies for surface-enhanced Raman scattering devices," *Analyst,* 10.1039/D1AN00624J vol. 146, no. 16, pp. 5008-5032, 2021, doi: 10.1039/D1AN00624J.

[136] M. Ringnér, "What is principal component analysis?," *Nature Biotechnology,* vol. 26, no. 3, pp. 303-304, 2008/03/01 2008, doi: 10.1038/nbt0308-303.

[137] [Online]. Available: Victor Lavrenko and Charles Sutton, 2011.

[138] R. Bro and A. K. Smilde, "Principal component analysis," *Analytical methods,* vol. 6, no. 9, pp. 2812-2831, 2014.

[139] H.-Y. Wang *et al.*, "Spindle-shaped microfluidic chamber with uniform perfusion flows," *Microfluidics and Nanofluidics,* vol. 15, no. 6, pp. 839-845, 2013/12/01 2013, doi: 10.1007/s10404-013-1195-8.

[140] M. G. Lee, S. Choi, and J.-K. Park, "Three-dimensional hydrodynamic focusing with a single sheath flow in a single-layer microfluidic device," *Lab on a Chip,* vol. 9, no. 21, pp. 3155-3160, 2009.

[141] H.-H. Wang *et al.*, "Highly Raman-Enhancing Substrates Based on Silver Nanoparticle Arrays with Tunable Sub-10 nm Gaps," *Advanced Materials,* vol. 18, no. 4, pp. 491-495, 2006, doi: https://doi.org/10.1002/adma.200501875.

[142] C. M. Ferreira, I. S. Pinto, E. V. Soares, and H. M. Soares, "(Un) suitability of the use of pH buffers in biological, biochemical and environmental studies and their interaction with metal ions–a review," *Rsc Advances,* vol. 5, no. 39, pp. 30989-31003, 2015.

[143] M. Morháč and V. Matoušek, "Peak Clipping Algorithms for Background Estimation in Spectroscopic Data," *Applied Spectroscopy,* vol. 62, no. 1, pp. 91-106, 2008/01/01 2008, doi: 10.1366/000370208783412762.

[144] D. Milanova, R. D. Chambers, S. S. Bahga, and J. G. Santiago, "Electrophoretic mobility measurements of fluorescent dyes using on-chip capillary electrophoresis," *ELECTROPHORESIS,* https://doi.org/10.1002/elps.201100210 vol. 32, no. 22, pp. 3286-3294, 2011/11/01 2011, doi: https://doi.org/10.1002/elps.201100210.

[145] P. O. Gendron, F. Avaltroni, and K. J. Wilkinson, "Diffusion Coefficients of Several Rhodamine Derivatives as Determined by Pulsed Field Gradient–Nuclear Magnetic Resonance and Fluorescence Correlation Spectroscopy," *Journal of Fluorescence,* vol. 18, no. 6, pp. 1093-1101, 2008/11/01 2008, doi: 10.1007/s10895-008-0357-7.

[146] P. Galambos and F. K. Forster, "Micro-Fluidic Diffusion Coefficient Measurement," in *Micro Total Analysis Systems '98*, Dordrecht, D. J. Harrison and A. van den Berg, Eds., 1998// 1998: Springer Netherlands, pp. 189-192.

[147] K. L. Geremia and P. G. Seybold, "Computational estimation of the acidities of purines and indoles," *Journal of Molecular Modeling,* vol. 25, no. 1, p. 12, 2019/01/03 2019, doi: 10.1007/s00894-018-3892-4.

[148] S. Ganguly and K. K. Kundu, "Protonation/deprotonation energetics of uracil, thymine, and cytosine in water from e.m.f./spectrophotometric measurements," *Canadian Journal of Chemistry,* vol. 72, no. 4, pp. 1120-1126, 1994, doi: 10.1139/v94-143.

[149] C. L. Benn *et al.*, "Physiology of Hyperuricemia and Urate-Lowering Treatments," (in eng), *Front Med (Lausanne),* vol. 5, p. 160, 2018, doi: 10.3389/fmed.2018.00160.

[150] Y. Nishikawa, T. Nagasawa, K. Fujiwara, and M. Osawa, "Silver island films for surface-enhanced infrared absorption spectroscopy: effect of island morphology on the absorption enhancement," *Vibrational Spectroscopy,* vol. 6, no. 1, pp. 43-53, 1993/10/01/ 1993, doi: https://doi.org/10.1016/0924-2031(93)87021-K.

[151] H. Nam, J. E. Park, W. Waheed, A. Alazzam, H. J. Sung, and J. S. Jeon, "Acoustofluidic lysis of cancer cells and Raman spectrum profiling," (in eng), *Lab Chip,* vol. 23, no. 18, pp. 4117-4125, Sep 13 2023, doi: 10.1039/d3lc00550j.

[152] W. Liu *et al.*, "Phenotyping Bacteria through a Black-Box Approach: Amplifying Surface-Enhanced Raman Spectroscopy Spectral Differences among Bacteria by Inputting Appropriate Environmental Stress," *Analytical Chemistry,* vol. 94, no. 18, pp. 6791-6798, 2022/05/10 2022, doi: 10.1021/acs.analchem.2c00502.

doi:10.6342/NTU202401456